

## Optical pumping technique for measuring small nuclear quadrupole shifts in $^1S_0$ atoms and testing spatial isotropy

S. K. Lamoreaux, J. P. Jacobs, B. R. Heckel, F. J. Raab, and E. N. Fortson  
*Department of Physics, FM-15, University of Washington, Seattle, Washington 98195*

(Received 26 August 1988)

Using  $^{201}\text{Hg}$  ( $I = \frac{3}{2}$ ) atoms, we have demonstrated a new technique for studying the static quadrupole interactions of nuclei in  $^1S_0$  atoms. The nuclear-spin precession frequency is made sensitive to quadrupole energy shifts by inducing, through optical pumping, both dipole and quadrupole spin polarization in a vapor of  $^{201}\text{Hg}$  atoms. The sensitivity predicted from measurements of the polarization agrees with the calibrated value found by inducing a known quadrupole light shift. By rotating the mercury-vapor cell, quadrupole interactions with the cell walls were observed with the expected  $\cos 2\phi$  azimuthal variation. In an application of this technique, a search for possible dependence of the  $^{201}\text{Hg}$  spin precession frequency on the orientation of the precession axis in space has yielded the null result  $\Delta f < 5 \times 10^{-7}$  Hz, which reduces the previous limits on spatial anisotropy by over three orders of magnitude and places stringent new bounds on violations of Lorentz invariance.

Nuclear quadrupole interactions have been studied by a variety of techniques, including molecular beams,<sup>1</sup> nuclear-magnetic and electric-quadrupole resonance,<sup>2</sup> and optical pumping.<sup>3</sup> For nuclei in  $^1S_0$  atoms, optical pumping (often in conjunction with spin exchange) is especially useful.<sup>4-6</sup> A limitation on all techniques has been the requirement that the quadrupole splitting be large enough to be resolved or at least to broaden a resonance line significantly. In this paper we describe a new optical-pumping technique we have developed for measuring quadrupole interactions when the splitting is far too small to be resolved. As already reported,<sup>7,8</sup> we have used this technique with  $^{201}\text{Hg}$  atoms to carry out the most exacting test yet of spatial isotropy. Other possible applications include measuring quadrupole shifts in large magnetic fields<sup>9</sup> and studying interactions with cell walls.<sup>6</sup>

In this technique both the dipole polarization and the alignment (quadrupole polarization) of the ensemble of nuclear spins play an important role. For example, a nonzero spin alignment means that a quadrupole splitting among the nuclear-spin levels causes not only a line broadening, but also a change in the weighted average of the energy of the levels and hence a line shift. In order to interpret a measured shift in terms of the strength of the quadrupole interaction of the nucleus, it is necessary to know the actual dipole and quadrupole spin polarization, or to calibrate the shift by inducing a known quadrupole interaction of the nucleus. We have demonstrated both procedures using direct optical pumping of mercury atoms. It should also be possible to establish calibration when spin-exchange pumping<sup>6</sup> is used to orient the nuclear spins, as in the case of noble-gas nuclei.

We divide the paper into the following sections: Sec. I, concept of the technique; Sec. II, theory of quadrupole frequency shifts; Sec. III, the experimental apparatus; Sec. IV, calibration of the quadrupole sensitivity; Sec. V, observation of wall relaxation and wall shifts; Sec. VI, ex-

perimental test of spatial isotropy and interpretation of results; Appendix A, solution to the spin- $\frac{1}{2}$  oscillator; and Appendix B, calculation of the induced light shift on a ground-state ensemble of atoms.

### I. CONCEPT OF THE TECHNIQUE

Suppose a sample of  $^1S_0$  atoms with nuclear spin  $I > \frac{1}{2}$  is placed in a magnetic field  $\mathbf{B}_0$  which causes a (dipole) shift in energy of the nuclear levels given by  $\hbar\omega_0 m_I$ , where  $m_I$  is the component of  $I$  along  $\mathbf{B}_0$ , and  $\omega_0$  is the Zeeman frequency shift (or Larmor frequency). If the atoms are subjected also to a quadrupole interaction, which for simplicity we assume has diagonal projection along  $\mathbf{B}_0$ , the levels will be shifted by an additional amount  $\hbar\omega_Q m_I^2$ , where  $\omega_Q$  is the quadrupole frequency splitting. The situation is illustrated in Fig. 1(a) for  $I = \frac{3}{2}$ . If  $\omega_Q$  exceeds the transverse spin-relaxation rate  $1/T_2$ , then the quadrupole splitting appears as three resolved lines in the usual  $\Delta m_I = \pm 1$  Zeeman transitions of nuclear magnetic resonance (NMR).

In this paper we are interested in the case when  $\omega_Q$  is so small that it is not resolved. The observable effect of an unresolved quadrupole interaction depends critically upon the experimental technique used. For example, in standard NMR the population difference between adjacent  $m_I$  levels is determined by the ratio  $\hbar\omega_0/kT$  in the Boltzmann factor and is almost independent of  $m_I$  in laboratory magnetic fields. All Zeeman transitions therefore have equal weight, leading to the line shapes shown in Fig. 1(b). The quadrupole interaction still splits the single Zeeman line at  $\omega_0$  into three equal amplitude lines separated by  $\omega_Q$ , but when these lines are not resolved there is no shift in the average frequency of the composite line. There is an increase in linewidth proportional to  $T_2\omega_Q^2$  which is of second order in the small quantity of interest  $\omega_Q$  and becomes very insensitive to quadrupole

interactions when  $\omega_Q \ll 1/T_2$ .

It is quite a different story if, as in Fig. 1(c), the population differences between adjacent  $m_I$  levels are not all the same. The sample then possesses, in addition to the dipole spin polarization  $\mathcal{D}$ , a quadrupole spin polarization which we call  $Q$ . As depicted in Fig. 1(c), there will be a shift in the line center  $\approx \omega_Q Q/\mathcal{D}$  that is of first order in  $\omega_Q$  and therefore can be much more sensitive to small quadrupole interactions than the line broadening is.

We use optical pumping to establish nuclear-spin polarization and to observe the frequency of spin precession about  $B_0$  by monitoring the modulated absorption of a transverse component of the light beam. An interesting aspect of optical detection is that since the light-absorption operator has a quadrupole component, it provides linear sensitivity to quadrupole shifts even when the atoms are polarized without alignment, as will be evident from the general expression for quadrupole sensitivity derived in Sec. II.

Our application of this technique to  $^{201}\text{Hg}$  has allowed us to detect quadrupole shifts  $\omega_Q$  smaller than a microhertz. Such high sensitivity is due to the long-spin-

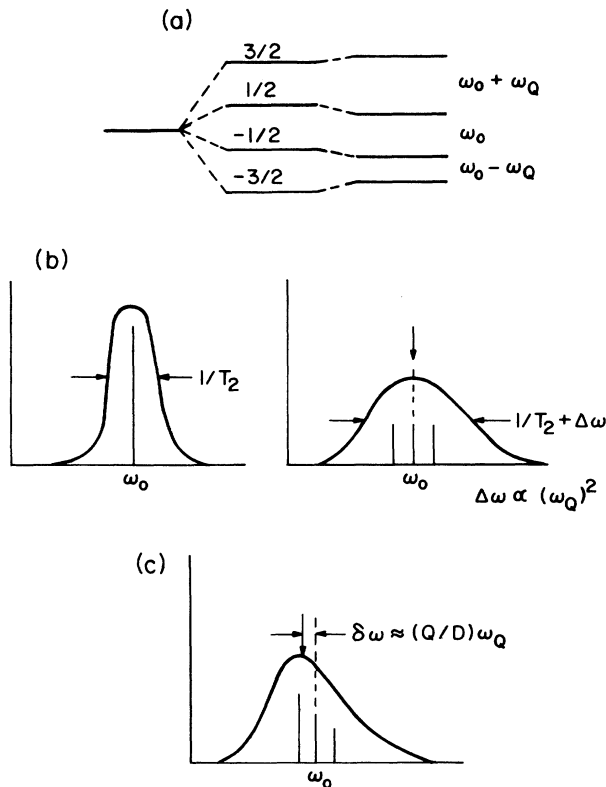


FIG. 1. (a) Atomic (nuclear) Zeeman levels are first split (equally) by a magnetic field, then further split (unequally) by a weak quadrupole interaction  $\omega_Q$ . If there are equal population differences between the adjacent Zeeman levels (represented by the vertical lines), the single NMR line becomes a triplet, and if  $\omega_Q < 1/T_2$ , the NMR line is broadened (b). When the sample has a quadrupole polarization, there will also be a shift in the line center (c).

relaxation time of the  $^1S_0$  atoms, and to the high signal-to-noise ratio that is generally available with optical pumping. With optical pumping it is also possible to use arbitrarily small magnetic fields without loss of signal, thereby reducing the constraints on fractional stability and uniformity of the field.

## II. THEORY OF QUADRUPOLE FREQUENCY SHIFTS

In this section we work out a detailed theory of the quadrupole frequency shift for an ensemble of spin- $\frac{3}{2}$  atoms such as  $^{201}\text{Hg}$  ( $F=I=\frac{3}{2}$ ). It is straightforward to treat any other spin ( $\geq 1$ ) in a similar way.

In our experiments we measure the quadrupole shifts by optically monitoring the precession of the spins about an axis along which the dipole, quadrupole, etc., energies are defined. We, therefore, develop the theory in a form for calculating both the rate at which the spins precess and the modulation they produce in a suitably directed and polarized light beam.

We assume there is a static magnetic field  $\mathbf{B}_0$  applied along the  $Z_0$  axis that produces a Zeeman splitting  $\omega_0 = \gamma B_0$ , where  $\gamma$  is the gyromagnetic ratio. In addition, we assume that there is a small quadrupole splitting  $\omega_Q$  along  $Z_0$ , where  $\omega_Q \ll \omega_0$ . The principal axes of the quadrupole interaction will not in general coincide with  $Z_0$  but because of the much larger Zeeman interaction only the components of the quadrupole energy which are diagonal along  $B_0$  will contribute to the total energy in first-order perturbation theory. To this order we can write the effective Hamiltonian as (suppressing  $\hbar$ )

$$H = \omega_0 m_F + \omega_Q \left[ \frac{m_F^2}{2} - \frac{5}{8} \right]. \quad (2.1)$$

The degree of symmetry of the quadrupole interaction and the orientation of its principal axes are manifest in how the observed quadrupole splitting  $\omega_Q$  in Eq. (2.1) varies with the orientation of  $\mathbf{B}_0$ . For example, if there is a symmetric quadrupole interaction with respect to an axis making an angle  $\alpha$  with  $Z_0$  and with splitting  $\omega_{Q\alpha}$  along that axis, then  $\omega_Q$  used in Eq. (2.1) is given by

$$\omega_Q = \frac{3 \cos^2 \alpha - 1}{2} \omega_{Q\alpha}. \quad (2.2)$$

The arguments of Sec. I could be repeated more quantitatively using Eq. (2.1). Thus the average energy  $\langle H \rangle$  will depend on  $\omega_Q$  only if its coefficient in Eq. (2.1) is not zero; that is, only if the spin alignment of the sample  $\langle (m_F^2/2) - \frac{5}{8} \rangle$  does not vanish along  $Z_0$ . Although we could calculate the frequency shift due to  $\omega_Q$  in this way, it is better for discussing our experiments to calculate the precession rate of the spins about  $Z_0$ .

To analyze the precession, we suppose that at time  $t=0$  the density matrix describing the ensemble is diagonal along an axis  $\hat{a}$  in the  $X_0 Z_0$  plane making an angle  $\theta$  with  $Z_0$ . The system could be prepared in this way by, for example, optically pumping with  $\mathbf{B}_0$  aligned with  $\hat{a}$  when  $t < 0$ , and then suddenly rotating  $\mathbf{B}_0$  to point along  $Z_0$  at time  $t=0$ .

We represent the density matrix in the  $\hat{a}$  basis by irre-

ducible spherical tensors;<sup>10</sup> for the spin- $\frac{3}{2}$  system, these tensors are represented by  $4 \times 4$  matrices,  $T_{LM}$ . The maximum order of the multipoles which represent the density matrix is 3 (octupole) since  $L_{\max} = 2F$  (see Appendix B). In the present case, only those  $T_{LM}$  with  $M_a = 0$  [Eq. (B1)] are needed to describe the density matrix since the off-diagonal terms are all zero. The density matrix (at  $t = 0$ ) is written as

$$\rho = \frac{1}{2}T_{00} + \mathcal{D}T_{10} + \mathcal{Q}T_{20} + \mathcal{O}T_{30},$$

where  $\mathcal{D}$ ,  $\mathcal{Q}$ , and  $\mathcal{O}$  represent the dipole, quadrupole, and octupole moments of the ensemble with respect to the  $\hat{a}$

axis.

It is easiest to perform calculations in the  $Z_0$  coordinate system, in which  $H$  is diagonal. The density matrix in this system is

$$\rho^0 = d^{3/2}(\theta)\rho d^{3/2}(-\theta),$$

where  $d^{3/2}(\theta)$  is the rotation operator. The time-evolution operator is

$$u(t) = e^{-iHt},$$

where, from Eq. (2.1),

$$H = \omega_0 \sqrt{5} T_{10}^0 + \omega_Q T_{20}^0 = \begin{pmatrix} 3\omega_0/2 + \omega_Q/2 & 0 & 0 & 0 \\ 0 & \omega_0/2 - \omega_Q/2 & 0 & 0 \\ 0 & 0 & -\omega_0/2 - \omega_Q/2 & 0 \\ 0 & 0 & 0 & -3\omega_0/2 + \omega_Q/2 \end{pmatrix}, \quad (2.3)$$

where the superscript on the  $T_{LM}$  indicates they are in the  $Z_0$  system, and we have ignored a  $T_{00}$  term which gives no information about the atomic polarization or frequency shifts (with our experimental technique). The time evolution of  $\rho^0$  is given by

$$\rho^0(t) = u(t)\rho^0 u^\dagger(t).$$

The evolution of the atomic ensemble is monitored with polarized light directed at some specified angle relative to  $Z_0$ . The polarization is described by the spherical basis vector

$$\hat{e} = (e_+, e_0, e_-)$$

defined in Appendix B. The change in transmitted light is described by the light-absorption operator<sup>4,10,11</sup> and can also be expanded in terms of the  $T_{LM}$  as discussed in Appendix B,

$$\mathcal{L}_{\mu\mu'}^A = \sum_m \langle \mu | \hat{e} \cdot \hat{D} | m \rangle \langle m | \hat{D} \cdot \hat{e} | \mu' \rangle,$$

where  $\hat{D}$  is the electric dipole moment operator,  $\hat{e}$  is the light-polarization vector,  $m$  labels the excited-state Zeeman level, and  $\mu$  and  $\mu'$  label ground-state Zeeman levels. For small fractional absorption, the light absorption is given by

$$\Delta I \propto \text{Tr}[\rho^0(t)\mathcal{L}_A].$$

The hyperfine line which we use for optical pumping couples the  $F = \frac{3}{2}$  ground state to the  $F = \frac{5}{2}$  excited state.  $\mathcal{L}_A$  can be readily calculated using the Wigner-Eckart theorem.

We find (for  $\omega_Q t \ll 1$ ),

$$\begin{aligned} \Delta I \propto & \left[ \frac{\mathcal{D} \sin \theta}{\sqrt{10}} (e_+^* e_0 + e_0^* e_-) + \frac{\mathcal{Q} \sin \theta \cos \theta}{5\sqrt{2}} (e_+^* e_0 - e_0^* e_-) \right] e^{i\omega_0 t} \\ & + \left[ \frac{\mathcal{D} \sin \theta}{5\sqrt{10}} (e_+^* e_0 - e_0^* e_-) + \frac{3\mathcal{Q} \sin \theta \cos \theta}{5\sqrt{2}} (e_+^* e_0 + e_0^* e_-) + \frac{\mathcal{O} \sin \theta (5 \cos^2 \theta - 1)}{10\sqrt{10}} (e_+^* e_0 - e_0^* e_-) \right] \omega_Q t e^{i(\omega_0 t - \pi/2)} \\ & + \left[ \frac{\mathcal{Q} \sin^2 \theta}{10} e_+^* e_- \right] e^{2i\omega_0 t} + \left[ \frac{\mathcal{O} \cos \theta \sin^2 \theta}{2\sqrt{5}} e_+^* e_- \right] \omega_Q t e^{i(2\omega_0 t - \pi/2)} + \text{c.c.}, \end{aligned} \quad (2.4)$$

where the components of  $\hat{e}$  are given in the  $Z_0$  coordinate system. For the important case of circularly polarized light ( $e_\pm$ ) propagating along an axis in the  $X_0 Z_0$  plane at an angle  $\beta$  relative to  $\hat{Z}_0$ , we have in the  $Z_0$  frame,

$$\begin{aligned} e_+^* e_0 + e_0^* e_- &= \pm \sin \beta / \sqrt{2}, \\ e_+^* e_0 - e_0^* e_- &= -\sin \beta \cos \beta / \sqrt{2}, \\ e_+^* e_- &= \sin^2 \beta / 4. \end{aligned} \quad (2.5)$$

The mathematical form of these equations comes about as follows. The time dependence of  $\rho^0$  is determined by  $[\rho^0, H]$ . As in Eq. (2.3), we can decompose the diagonal matrix  $H$  by means of irreducible tensor operators

$$H = h_0 T_{00} + h_1 T_{10} + h_2 T_{20} . \quad (2.6)$$

$T_{00}$  commutes with  $\rho^0$  and produces no measurable effect.  $T_{10}$  behaves like the rotation operator  $J_z$  in all commutation relations. Hence the  $h_1$  term will cause individual multipoles of  $\rho^0$  to precess but preserves multipolarity. However, multipole operators of rank  $\geq 2$  mix the multipole moments of  $\rho^0$  with different  $L$ . When there is any quadrupole interaction ( $h_2 \neq 0$ ), population is transferred between the various multipoles with  $\Delta L = \pm 1$  at a rate which depends linearly on  $h_2$ .

The physical significance of Eq. (2.4) can now be seen. The new dipole polarization

$$(3Q \sin\theta \cos\theta / 5\sqrt{2})\omega_Q t$$

generated from the quadrupole polarization adds to the original dipole polarization but with a  $90^\circ$  phase shift. The same is true for all multipoles mixed by the quadrupole interaction, resulting in the  $\sin(\omega t)$  term in Eq. (2.4). This population redistribution thus produces a phase shift in the precessing moments which increases linearly in time, thereby effectively changing the precession frequency of the system. It is interesting that it is not necessary to have an initial quadrupole (or octupole) in the sample to be linearly sensitive to quadrupole energy shifts. This is because the light monitors both the dipole and quadrupole multipoles, including the quadrupole generated from the dipole polarization by  $\omega_Q$ .

To obtain an expression for the change  $\delta\omega_Q$  in precession frequency due to the quadrupole interaction, we write the first two terms of Eq. (2.4) as

$$\begin{aligned} \Delta I &= C_1 \cos\omega_0 t + C_2 \omega_Q t \sin\omega_0 t , \\ &\cong C_1 \cos(\omega_0 - \delta\omega_Q) t , \end{aligned}$$

where

$$\delta\omega_Q \cong \frac{C_2}{C_1} \omega_Q .$$

As an example, when  $\theta = 45^\circ$  and we use  $e_+$  light directed at an angle  $\beta = 45^\circ$ , we find (letting  $\theta = 0$ )

$$\delta\omega_Q = \frac{2 + 6\sqrt{5}Q/D}{10\sqrt{2} + \sqrt{10}Q/D} \omega_Q . \quad (2.7)$$

This equation or similar ones deduced from Eq. (2.4) are useful for estimating  $\delta\omega_Q/\omega_Q$  when  $D$  and  $Q$  can be measured under operating conditions. However, our simplified precession model describes only approximately the driven atomic light-absorption oscillators used in our experiments, and it is therefore best to directly calibrate the sensitivity by introducing known quadrupole (and dipole) interactions as described in Sec. IV. Finally, although we discuss only the frequency-shift technique we have exploited, there are other methods implicit in Eq. (2.4) for detecting the effect of  $\omega_Q$ .

### III. EXPERIMENTAL APPARATUS

The apparatus we have used to study quadrupole energy shifts consists of  $^{199}\text{Hg}$  and  $^{201}\text{Hg}$  atomic light-absorption oscillators, which are based on the nuclear-spin precession frequency of each isotope.<sup>12,13</sup> The  $^{199}\text{Hg}$  isotope with nuclear spin  $I = \frac{1}{2}$  (no quadrupole moment) is used to stabilize the external magnetic field leaving the  $^{201}\text{Hg}$  atomic oscillator sensitive only to quadrupole energy shifts (and nonmagnetic dipole energy shifts). To calibrate the system, a known quadrupole light shift is induced in the  $^{201}\text{Hg}$  atoms by off-resonance light from a  $^{200}\text{Hg}$  lamp. The calibration of the apparatus for both quadrupole and dipole shifts is discussed fully in Sec. IV. We first summarize the principle of the atomic oscillators, then describe the layout and operation of the experiment, and finally present a more detailed description of each part of the apparatus.

#### A. The atomic oscillators

A schematic diagram of the experimental apparatus is given in Fig. 2. The atomic oscillators operate with the geometry shown in the top portion of the figure. Circularly polarized resonance light propagates along the  $z$  axis. At an angle of  $45^\circ$  to  $z$  is a static magnetic field  $\mathbf{B}_0$ , which defines the quantization or precession axis (the  $Z_0$  of Sec. II) and defines the  $z_E$  axis of the experiment coordinate system, shown in Fig. 3. Along the  $y$  axis is an oscillating magnetic field  $B_1$  whose frequency  $\omega$  is close to the Larmor frequency  $\omega_0 = \gamma B_0$  (actually there are two frequencies, one for each isotope). (To test for spatial isotropy, the apparatus is oriented so that  $y$  is parallel to the Earth's rotation axis;  $\mathbf{B}_0$  is thus parallel to the Earth's equatorial plane, and the direction of  $\mathbf{B}_0$  in space changes as the Earth rotates. See Sec. VI.)

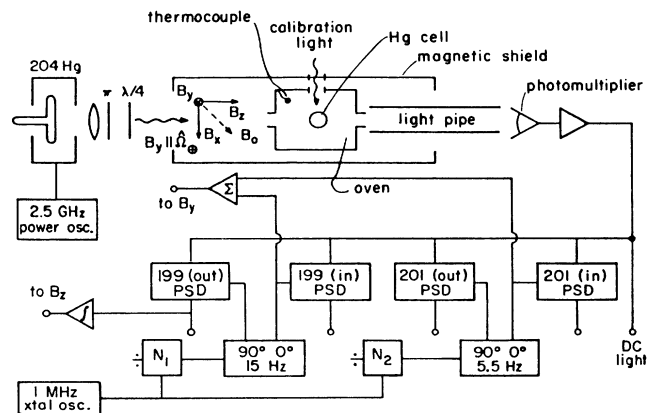


FIG. 2. Schematic of the apparatus. A set of three coils within the magnetic shields is used to generate magnetic fields in the three mutually orthogonal directions, labeled here for convenience as  $B_x$ ,  $B_y$ , and  $B_z$ .  $B_x$  and  $B_z$  are equal-magnitude static fields. The magnetic field stabilizer feeds back only to  $B_z$ .  $B_y$  is the rf field, and in the test of spatial isotropy is aligned with the Earth's rotation axis.

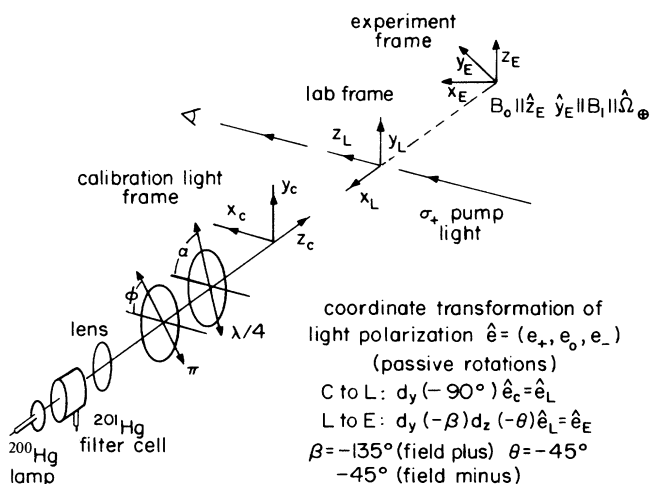


FIG. 3. Experimental setup for calibrating the apparatus through use of the virtual light shift. The  $xyz$  frame of Fig. 2 is obtained from the  $L$  frame by simply rotating by  $45^\circ$  about  $z_L(z)$ . Equivalently, the  $E$  frame is obtained from the  $xyz$  frame by rotating by an angle  $-\beta$  about  $y(y_E)$ .

The projection of the light along  $\mathbf{B}_0$  optically pumps a polarization of the nuclear spins which would be oriented along  $\mathbf{B}_0$  in the absence of  $B_1$ . The effect of  $B_1$  is to create a component of spin polarization perpendicular to  $\mathbf{B}_0$  that precesses about  $\mathbf{B}_0$  at the frequency of  $B_1$ . The projection of spin polarization along the light direction  $z$  therefore has an oscillating part, including a modulation in the transmitted light intensity at frequency  $\omega$ .

Close to resonance, when  $\omega \approx \omega_0$ , the modulation has approximately the same phase as  $B_1$ . The out of phase (quadrature) component of modulation then becomes sensitive to shifts in the spin-resonance frequency. In particular, a quadrupole frequency shift  $\delta\omega_Q$ , as given for example in Eq. (2.7), will show up as a phase shift in the modulation signal of magnitude  $\phi_Q \approx T_2 \delta\omega_Q$ , where  $T_2$  is the transverse spin-relaxation time. The quadrature light-modulation signal is thus used to measure energy shifts while the in-phase signal is used to monitor the total-modulation amplitude.

### B. Layout and operation of the experiment

The source of the resonant pumping light is a stabilized  $^{204}\text{Hg}$  electrodeless microwave discharge lamp. The single 253.7-nm line of the  $^{204}\text{Hg}$  overlaps the  $F = \frac{1}{2}$  to  $F = \frac{1}{2}$  transition in  $^{199}\text{Hg}$  and the  $F = \frac{3}{2}$  to  $F = \frac{5}{2}$  transition in  $^{201}\text{Hg}$ . The resonance light is linearly polarized by reflection from a quartz plate oriented at Brewster's angle. This linear polarization is converted to circular polarization by a quartz-compression quarter-wave plate. The intensity of the lamp is monitored by detecting the (lost) light transmitted through the Brewster plate with an ultraviolet sensitive  $p$ - $i$ - $n$  photodiode.

The light intensity at the cell is adjusted by use of an

aperture. For the particular cell used in these experiments, the intensity is set so that the  $^{199}\text{Hg}$  spin-relaxation lifetime is reduced to 80 sec and the  $^{201}\text{Hg}$  lifetime to 50 secs. The lifetimes in the dark are 1000 and 80 secs, respectively.

The cell is a 2-cm-diam quartz sphere which contains natural Hg vapor at the  $0^\circ$  vapor pressure. It is located in an oven (about  $300^\circ\text{C}$ ) in the center of a set of magnetic field coils. This assembly is surrounded by three concentric cylindrical Molypermalloy magnetic shields.

The magnitude of the static field  $\mathbf{B}_0$  is set at 20 mG, corresponding to Larmor frequencies for the  $^{201}\text{Hg}$  and  $^{199}\text{Hg}$  of 5.5 and 15 Hz, respectively. The oscillating field  $\mathbf{B}_1$  for each isotope is an amplitude-controlled square wave. The higher harmonics of the square waves are well outside the linewidths (about 10 mHz) of each isotope. The amplitude of the oscillating field for each isotope is set so that the in-phase signals (the transmitted light modulation in-phase with  $B_1$ ) are 0.7 times their limiting (maximum) values. For the  $^{201}\text{Hg}$  this corresponds to about  $19 \mu\text{G}$  and for the  $^{199}\text{Hg}$  about  $6 \mu\text{G}$ .

A polished aluminum light pipe collects the light transmitted through the cell. The intensity of the transmitted light is measured with a solar-blind photomultiplier (PM) tube. The signal from the PM is passed through a bandpass amplifier and then is phase detected against the oscillating ( $B_1$ ) fields. There are two phase-sensitive detectors (PSD's) for each isotope; one for the in-phase component and one for the quadrature component of the signal. Since any shift in precession frequency appears as a phase shift, it is necessary to have control over all electronically induced phase shifts, hence the use of digital electronics wherever possible. The in-phase and quadrature PSD reference signals and the oscillating field drive signals are all generated digitally.

The  $^{199}\text{Hg}$  quadrature signal is used to stabilize the magnetic field. The output of the PSD which detects the quadrature signal is electronically integrated. This signal is added to the  $B_z$  coil quiescent current. The phase is set so that the feedback is negative, and the gain is set so that the loop is slightly underdamped. Because the  $B_1$  frequencies for the two isotopes are derived from the same quartz-crystal oscillator, and since the static magnetic field is stabilized with the  $^{199}\text{Hg}$  quadrature signal, the  $^{201}\text{Hg}$  quadrature signal is insensitive to fluctuations in the magnetic field due to drifts in the reference oscillator. Also, there is no net field drift between the two isotopes since they are in the same cell and average the same volume many times in a nuclear-spin lifetime.

The  $^{201}\text{Hg}$  quadrature signal is a measure of a relative shift between the resonance frequencies of the two isotopes for a dipole energy shift that is not in the ratio of the magnetic moments and a direct measure of a quadrupole energy shift (since a quadrupole cannot affect the  $^{199}\text{Hg}$ ) up to some calibration coefficients. The determination of these coefficients is fully described in Sec. IV.

The light used to induce a quadrupole shift for calibration is generated by a  $^{200}\text{Hg}$  lamp (the single line does not overlap any transitions in the 201 or 199 isotopes) similar to the one used for pumping. The calibration light is polarized with a UV-105 polarizer and a quartz-

compression quarter-wave plate. This light enters the shield, oven, and cell perpendicular to  $z$  (see Fig. 3).

The in-phase and quadrature signals, light intensity, field-correction signal, oven current, room temperature and, in the anisotropy experiment, the time of day are all digitized by a computer. The digitized signals are averaged for 60 sec intervals, and then displayed on a terminal and recorded by the computer.

### C. Lamp fabrication

The lamps used for optical pumping and calibration are both made the same way. The design and techniques of fabrication are similar to those described in Ref. 14.

The lamp bulb is a quartz disk which is 25 mm in diameter, 5 mm deep, with approximately 0.5-mm-thick walls. The entrance to the 50-mm-long by 3-mm-diam stem has a 1-mm constriction to help keep the discharge confined to the bulb.

The lamp blanks are attached to a quartz tube which connects to a Pyrex  $U$  tube that serves as a liquid- $N_2$  cold trap. Between the lamps and the cold trap is a Pyrex sidearm with another  $U$  tube that serves as a dry-ice cold trap, followed by a Pyrex magnetic hammer pigtail break-seal ampoule which contains the enriched Hg isotope (either 200 or 204) in the form of mercuric oxide (HgO). The entire assembly is attached to a vacuum system equipped with a Pyrex flask filled with spectroscopically pure argon, a Hg closed-end manometer, and an ion vacuum gauge. The system is then pumped down to  $5 \times 10^{-7}$  torr.

The lamps are heated in an oven to 950°C while the ampoule and dry-ice cold trap are heated to 400°C in an adjoining oven. The ovens are held at this temperature for about 4 h. After the system cools to room temperature, 2 torr of Ar is admitted to the lamps for further cleaning with an rf discharge. The discharge is maintained in each lamp for an hour, during which time the Ar is changed periodically. Finally, the lamps are again pumped down to  $5 \times 10^{-7}$  torr.

The HgO ampoule is then opened by breaking the pigtail seal. The dry-ice-cold-trap Dewar is then filled with a dry-ice-acetone slurry. The HgO powder is heated until an increase in pressure is seen on the ionization gauge. The HgO is decomposed at a rate such that the pressure remains below  $10^{-4}$  torr (about 45 min for 2 mg). The slow decomposition ensures that the Hg condenses in the dry-ice cold trap.

After all of the HgO has decomposed the dry ice is removed. When the trap approaches room temperature the lamps and Hg are closed off from the rest of the system with a stopcock. The lamps are placed in liquid nitrogen, and the glassware is gently heated (40°C) to drive the Hg into the lamps. After the Hg has condensed in the lamps, they are allowed to warm to room temperature at which time 2 torr of Ar is admitted. The lamps are then sealed off containing the Ar and Hg. It was found that having 2 torr of Ar greatly improves lamp stability, increases the lamp lifetime, and makes starting the discharge easier. Lamps fabricated according to these plans provide about 1000 h of useful service.

### D. Cell fabrication

The Hg optical-pumping cell is fabricated on the same vacuum system as the discharge lamps. The cells are fabricated from high-purity synthetically produced fused-silica tubing (Heraeus-Amersil Suprasil I) 22 mm i.d.  $\times$  24 mm o.d. Before the tubing is heated, it is cleaned by rinsing with methanol and distilled water. The tubing is shaped into a 22-mm-diam sphere with approximately 1-mm-thick walls and a 50-mm stem which is 3 mm in diameter.

We made four cells according to the following recipe. The cells are attached to a fused-silica tube which is attached to a Pyrex  $U$  tube that serves as liquid- $N_2$  cold trap. There is a Pyrex sidearm between the cells and the cold trap which has the magnetic hammer pigtail break-seal ampoule containing about 1 ml of natural Hg (high-purity, distilled under vacuum). Since cleanliness is of utmost importance when attempting to get long-spin lifetimes, all of the tubing after and including the cold trap is new and has been cleaned with acetone and distilled water prior to fabrication. Just before the cold trap there is a constriction in the Pyrex tubing which allows the cells and ampoule to be "sealed off" easily from the rest of the system. As the system is evacuated, the liquid-nitrogen-cold-trap Dewar is filled. As the system pumps down, the cells and ampoule are heated in ovens to 350°C and held there for 6 h. During this time, the pressure comes down to about  $6 \times 10^{-6}$  torr. After the ovens cool and are removed, the seal-off areas on the cells are heated until nearly at the fused-silica softening point (nearly white hot), and the Pyrex seal-off is heated just to the softening point. The oven surrounding the cells is replaced and heated to 950°C and held there for 8 h. When the temperature cools to 300°C, the Hg ampoule is opened. The Hg is pumped for a few minutes until the pressure returns to its initial value. The ampoule-cell assembly is then sealed off from the rest of the system. The cells, exposed to Hg vapor at the room-temperature vapor pressure, were cycled daily between 600 and 100°C for five days. It has long been known that thermally cycling cells in the presence of the vapor increases the lifetime.<sup>15,16</sup>

The Hg ampoule is placed in a 0°C ice bath and the cells are cycled to 600°C once more. The cells are sealed off from the system one at a time. Between each cell sealoff, the remaining cells are cycled up to 600°C.

In the one batch we made according to this recipe, the first cell had an 80-sec relaxation time for the  $^{201}\text{Hg}$  which gradually deteriorated. This deterioration could have been caused by irradiating the cell with ultraviolet light when it was not heated. The second cell we removed was kept at 300°C whenever exposed to uv light. It has been working with an undiminished lifetime for nearly two years of intermittent use (2000 h) and has a lifetime of 80 sec for  $^{201}\text{Hg}$  (dipole lifetime) and over 1000 sec for the  $^{199}\text{Hg}$  lifetime. The cell lifetimes are fully discussed in Sec. V.

### E. Lamp drivers

There are two lamp drivers used in the apparatus: one for the pumping light ( $^{204}\text{Hg}$ ) and the other for the cali-

bration light ( $^{200}\text{Hg}$ ). The pumping lamp is driven by microwave power generated by a Hitachi 2M53A microwave-oven magnetron. The lamp is placed in a section of  $5.5 \times 9.6 \text{ cm}^2$  rectangular waveguide 36 cm long constructed of  $\frac{1}{16}$  in. sheet copper. The ends of the waveguide are closed. The magnetron antenna sticks into the cavity  $\frac{1}{4}$  of a free-space wavelength at a point  $\frac{1}{4}$  of a guide wavelength from one closed end while the lamp is located  $\frac{1}{4}$  of a guide wavelength from the other closed end. The lamp bulb is located near the waveguide wall (magnetic coupling) with the stem outside the cavity. The opposite side of the cavity has a slot to allow the light to exit. Having the lamp in this position confines the discharge to the bulb leaving the stem unlit.

We found that the lamp gave more stable operation if the discharge was kept out of the stem and if the stem was kept at a constant temperature. The stem temperature was regulated by a thermoelectric (Peltier) cooler and a thermistor configured in a feedback circuit at  $14^\circ\text{C}$ . We also found that blowing a stream of hot air across the bulb face ( $100^\circ\text{C}$ ) improved lamp stability.

The magnetron filament, which floats at  $-3000 \text{ V}$ , is powered by a 3.14-V dc 14-A power supply that is regulated to 1%. The anode current, about 20 mA, is also regulated. The output light intensity shows no discernable 60-Hz modulation. However, there is still some lower-frequency noise greater than shot noise.

Under normal operating conditions, the discharge must be initiated with a high-frequency spark. We use a xenon flashlamp trigger circuit. The lamp stabilizes after about 24 h of running. We have noticed considerable drift in the output intensity of new lamps for about the first 100 h of operation ( $-2\%$  per day). After the lamp is "aged," this drift decreases ( $-0.2\%$  per day).

The calibration lamp is driven by a microwave discharge which is very similar to the one just described. The microwaves are generated by a diathermy magnetron (Raytheon RK5609) which drives a foreshortened coaxial resonator.<sup>17</sup> Again, the magnetron anode current and filament voltage are regulated. Because the calibration lamp is only used for short periods of time, the long-term stability is not as critical as in the case of the pumping lamp. For this reason the stem of the calibration lamp is not cooled, and the bulb is not heated.

#### F. Light polarization

The pump light is linearly polarized by reflection from a stack of three Suprasil fused-silica plates 3 in. in diameter and  $\frac{1}{16}$  in. thick located at Brewster's angle. There is a small gap and a smaller angular offset between each plate (0.001 in. on one side, 0.002 in. on the other) to reduce interference between reflection from the various surfaces. The degree of polarization is at least as high as commercially manufactured Polacoat UV-105 polarizer, and the "transmission" is higher. The degree of polarization is relatively insensitive to variations in the angle near the Brewster angle. Thus, alignment is not terribly critical ( $3^\circ$  accuracy is quite adequate). However, it is difficult to rotate the polarization when using the Brewster plate. For this reason, we use a UV-105 linear polar-

izer for the calibration light, as described in Sec. IV.

The linear polarization is converted to circular polarization by a quartz-compression quarter-wave plate.<sup>14</sup> It consists of a sheet of fused silica about  $3 \times 3 \text{ in.}^2$  and  $\frac{1}{4}$  in. thick. There is a fixture which applies an even pressure along the plate through adjustment screws which press on neoprene pads located on either end of the plate. The plate is adjusted by tightening or loosening the screws while monitoring the maximum and minimum intensity as a UV-105 polarizer is rotated between the output light and the R166 detector. Note that it is impossible to determine the sense of circular polarization with these measurements. We rely on light-shift calculations to determine this. In first order, the axis of the plate which receives the pressure becomes the slow axis.

These plates are stable if treated gently. However, there is some evidence that the adjusted plate drifts over time. Mechanical shocks can also alter the adjustment.

#### G. Light pipe and photomultiplier

The light pipe is made from a length of seamless smooth-wall aluminum tubing 1 in. in diameter. The inside surfaces are polished using a commercial compound (Simichrome polish). The tube is rinsed with acetone and methanol after polishing. About 20% of the incident light (if less than  $20^\circ$  divergence) is transmitted by the 18-in tube. The light is detected with a solar-blind Hamamatsu R-166 photomultiplier with a quantum efficiency of between 10% and 20%. The dark current from the PM is low enough to be negligible compared to shot noise.

A United Detector Technology UDT-UV100 *p-i-n* photodiode detector is used to monitor the dc light output from the lamp, by viewing the light transmitted through the Brewster plate. A liquid filter is used to block the visible light as described in Ref. 18. Although this detector has a higher quantum efficiency than the R166, its noise output was much greater.

#### H. Magnetic field coils and shielding

There are three sets of magnetic field coils, one for each axis. For convenience, we label them  $B_x$ ,  $B_y$ , and  $B_z$ , which should not be confused with the axes defined in Sec. IV or Fig. 3. These coils are wound on a Plexiglas cylinder 7.5 in. in diameter and about 20 in. long.  $B_y$  is generated by a single-wire cylindrical Helmholtz coil.  $B_z$  is generated by a series of planar loops about the cylinder at 1 in. spacings. The leads to each loop are arranged in such a way that they do not contribute to the magnetic field.  $B_x$  is generated by a 30-turn "cosine" distribution winding; loops of wire run along the cylinder at angular increments given by  $\theta_n = \pm \arccos[(N+1-2n)/N]$ , where  $N$  is an even number,  $n = 1$  to  $N$ , similar to a cylindrical Helmholtz windings. There is a hole in the Plexiglas form for the calibration light.

As discussed in Appendix A, any misalignment of the oscillating field from perpendicular relative to the plane described by the light and static magnetic field will lead to phase offsets in the atomic oscillators. This means that

the coils must be wound accurately, and they must be stable. We estimate that the angles are accurate to about  $2^\circ$ , which gives an apparent frequency offset of  $110 \mu\text{Hz}$ . This is about how accurately we can set the drive frequency of the  $^{201}\text{Hg}$  relative to the  $^{199}\text{Hg}$  (due to the step size in the divider chain).

The magnetic shields are three concentric cylindrical Molypermalloy cylinders whose walls are  $\frac{1}{16}$  in. thick. The innermost shield is 7.5 in. in diameter by 20 in. long, the next shield, 9 in. by 27 in., and the outermost, 11 in. by 42 in. There are endcaps which fit over the end of each cylinder and overlap for about 2 in. Each endcap has a 2.5-in.-diam. hole. There are two 1-in. holes in the sides of the cylinders at the midpoint along the length located on opposite sides. When the shields are assembled, the holes line up so that there is a clear path into the shields for the calibration light.

The shielding factor for small magnetic fields transverse to the axis of the shield was measured to be 34 000. By use of a ten-loop demagnetization coil a residual field of  $< 10 \mu\text{G}$  can be achieved at the center of the shields.

#### I. PSD reference generator

The PSD's require  $0^\circ$  and  $90^\circ$  phase signals relative to the oscillating field  $B_x$ . Starting with a 1 MHz reference, a programmable divide-by- $N$  counter generates a square-wave train at twice the desired frequency. Flip flops, appropriately phased, then divide by 2 to generate the in-phase and quadrature references. There are two divider circuits, one for each isotope.

The  $0^\circ$  signal is used to drive the oscillating field. Each frequency amplitude is set to the appropriate value with  $10 \text{ k}\Omega$  ten-turn potentiometer. The frequency components are added, and any dc offsets filtered off. We use high-precision metal-film resistors and Mylar capacitors in the critical filter elements to minimize phase drifts. The low-frequency cutoff of the high-pass filter is below the frequencies of interest by more than a factor of 100.

#### J. Detection electronics

The anode current from the photomultiplier which detects the light transmitted by the cell is converted to a voltage in a  $1 \text{ V}/\mu\text{A}$  current follower with a high-frequency cutoff of 1 kHz. The dc component is filtered out with a 0.01-Hz high-pass filter. The signal is amplified by an adjustable gain amplifier.

At this point the signal is split and sent into two sets of phase-sensitive detectors (PSD's) that were specifically designed for low phase drift. There is one set of PSD's for each optically pumped isotope, and each set consists of two PSD's; one for the in-phase and one for the quadrature signal. The reference circuit described in the preceding section provides the in-phase and quadrature reference for the PSD's. A complete description of these PSD's can be found in Ref. 8.

The dynamic rejection of the PSD's is  $-65 \text{ dB}$ . The phase drift is less than  $10^{-5} \text{ rad/h}$ , as measured by having a large in-phase signal and monitoring the out-of-phase drift.

The oscillator drive frequencies are adjusted to give zero quadrature signal. Due to small electronic and optical-alignment errors, the drive is not exactly on resonance. However, it is typically within 0.01 linewidths, and possible drifts in these offsets are accounted for in the data analysis.

#### K. Magnetic field current source and stabilizer

When the atomic oscillator is operating very near resonance, the quadrature signal is near zero and approximately linear. This fact allows us to use the  $^{199}\text{Hg}$  quadrature signal in a servo system to stabilize the magnetic field by adding or subtracting from the static  $B_z$  field to hold the  $^{199}\text{Hg}$  quadrature signal at zero.

The current through each coil is controlled with a high-quality ten-turn wire-wound variable resistor. The field windings are calibrated to within 1% in  $\text{mG}/\text{mA}$  using a flux-gate meter. The resistors are adjusted so that the magnetic field is of the correct amplitude (15 and 5.5 Hz Larmor frequencies for each isotope) and at the right angle ( $B_x = B_z$ ,  $45^\circ$  to the light). The current is supplied by a 12-V storage battery that is charged by a precision adjustable supply, such that the current out of the supply is exactly equal to the current out of the battery. The battery works like a huge capacitor and tends to reduce noise from the supply. The total current is about 20 mA.

#### L. The oven

To get long atomic-spin lifetimes in a cell, the cell must be kept in an oven at about  $300^\circ\text{C}$ . The oven is a double-walled cube of 5-in. outside edge and 3-in. inside edge. Between the walls is Fibrefrax insulation (aluminum oxide fiber blanket, manufactured by Carborundum). The heating element is made from Amperex Thermocoax wound on a ceramic cylinder. Coaxial heater wire is used to reduce the magnetic field generated by the heater current. The cell is supported by its stem, which protrudes into a ceramic tube that is coaxial with the heater cylinder. The ceramic tube passes through the bottom of the oven and through the insulation and is supported from the outside. There is a pulley attached to the bottom of the ceramic tube. A nylon cord runs around the pulley and to the outside of the magnetic shields allowing the cell to be rotated without disturbing the magnetic shields, oven, etc.

The temperature of the oven is monitored with a copper-constantan thermocouple. The reference junction is kept in a  $0^\circ\text{C}$  ice bath. The oven temperature is controlled by comparing the thermocouple voltage to an adjustable reference voltage. The error signal is used to control the duty cycle of a 10-kHz square wave which supplies the power to the heater winding. Under normal operating conditions, the heater draws about 1.5 A at 20 V ac.

There is no observable change in the thermocouple voltage over the period of a day; however, there is the possibility of temperature-gradient variations. The thermocouple measures the temperature at only one point in the oven, midway between the cell and oven wall. We estimate that the internal temperature-gradient variations

are probably a factor of at least 100 less than the external total temperature changes. We base this estimate on the insulation thickness and take into account the constant-temperature internal aluminum box.

We also measure the heater current of which there is a diurnal variation. Since the coaxial heater wire is wound in a helix, it no longer has the axial symmetry necessary to cancel the field external to the wire. The leakage field of the heater is about 2 mg/A and agrees with a calculation using the dimensions of the wire and cylindrical form. Since the ac field affects each isotope in a ratio different from the ratio of the  $g$  factors (Bloch-Siegert shift), the magnetic field stabilization will not cancel its effects. This is a possible source of systematic error which we will further consider in Sec. VI B.

#### IV. CALIBRATING THE APPARATUS

We wish to know the dipole and quadrupole sensitivity of our apparatus, namely, the change in Hg atomic oscillator phase (as measured by the quadrature signal) for a given dipole or quadrupole energy shift among the ground-state Zeeman levels. This signal depends on the precessing dipole, quadrupole, and octupole polarizations of the atomic ensemble [cf. Eq. (2.7)], which in turn depend in a complicated way upon the pumping light,  $B_1$  driving field, and nuclear-spin relaxation. Calculating the sensitivity is at best a difficult problem. Instead we calibrate the apparatus by applying known energy shifts, using the magnetic field splitting (or simply changing the oscillator drive frequency) for the dipole calibration, and using the virtual light shift (ac Stark effect) for the quadrupole calibration.

In this section, after sketching the dipole calibration procedure for  $^{199}\text{Hg}$  and  $^{201}\text{Hg}$ , we analyze in some detail the more involved  $^{201}\text{Hg}$  quadrupole calibration technique. We then present results of direct measurements of the precessing dipole and quadrupole polarization, which provide a check on the calibrated quadrupole sensitivity. Finally, we briefly compare the measured sensitivity with results of a numerical calculation.

##### A. The $^{199}\text{Hg}$ and $^{201}\text{Hg}$ dipole calibrations

The Hamiltonian for the dipole and quadrupole energies of the  $^{201}\text{Hg}$  ensemble is given by Eq. (2.3), which we write here in the form

$$H_{201} = (\gamma_{201}B + E_d)\sqrt{5}T_{10}(\frac{3}{2}) + E_Q T_{20}(\frac{3}{2}), \quad (4.1)$$

where the  $T_{i0}(\frac{3}{2})$  are given by Eq. (B1),  $E_d$  is any dipole energy besides the magnetic Zeeman energy, and  $\gamma_{201}$  is the magnitude of the  $^{201}\text{Hg}$  gyromagnetic ratio [the negative sign of this ratio for  $^{201}\text{Hg}$  is taken into account in Eq. (4.1)]. We may write the Hamiltonian for  $^{199}\text{Hg}$  simply as

$$H_{199} = (-\gamma_{199}B + E'_d)T_{10}(\frac{1}{2})/\sqrt{2}. \quad (4.2)$$

The quadrature signal from the  $^{199}\text{Hg}$  oscillator is used to provide a correction voltage  $V_{\text{corr}}$  to stabilize the magnetic field. Thus the  $^{199}\text{Hg}$  drive frequency  $f^{199}$  is given by

$$f^{199} = |(-\gamma_{199}|\mathbf{B}_0 + \delta\mathbf{B}| + E'_d)|/2\pi = \text{const} \quad (4.3)$$

where  $\delta\mathbf{B}$  is the magnetic field correction (applied along the  $z$  axis at  $45^\circ$  to  $\mathbf{B}_0$ ). We measure  $\alpha_m$ , the calibration factor between  $\delta B_z$  and  $V_{\text{corr}}$

$$\alpha_m \equiv \delta B_z / \delta V_{\text{corr}} = \sqrt{2} \delta B / \delta V_{\text{corr}}.$$

For our apparatus, we find  $\alpha_m = 48.25$  nG/bit. (We measure voltages in analog-to-digital bits; 1 V = 204.8 bits.) Thus by monitoring  $V_{\text{corr}}$  we determine any dipole energy shift among the  $^{199}\text{Hg}$  sublevels.

In the case of the  $^{201}\text{Hg}$  oscillator, we define a dipole calibration factor  $\xi$  as the inverse of the sensitivity of the quadrature signal (out-of-phase voltage  $V_{\text{out}}^{201}$ ) to a dipole energy shift

$$\frac{\partial V_{\text{out}}^{201}}{\partial E_d} = \xi^{-1}. \quad (4.4)$$

We measure  $\xi$  by changing the  $^{201}\text{Hg}$  oscillator drive frequency by a small amount  $\Delta f^{201} = 120$   $\mu\text{Hz}$  and measuring the response  $\Delta V_{\text{out}}^{201}$ . Since increasing the drive frequency is equivalent to decreasing the magnetic field,

$$\xi = -\frac{\Delta f^{201}}{\Delta V_{\text{out}}^{201}}.$$

$\xi$  is typically about 3  $\mu\text{Hz/bit}$ .

##### B. The $^{201}\text{Hg}$ quadrupole calibration by the virtual light shift

To specify the quadrupole sensitivity, it is convenient to introduce a dimensionless parameter  $\eta$ , the ratio of the quadrupole to dipole sensitivity,

$$\eta \equiv \frac{\partial V_{\text{out}}^{201}}{\partial E_q} / \frac{\partial V_{\text{out}}^{201}}{\partial E_d} = \xi \frac{\partial V_{\text{out}}^{201}}{\partial E_q}. \quad (4.5)$$

We determine  $\eta$  through use of the virtual light shift induced on the  $^{201}\text{Hg}$  and  $^{199}\text{Hg}$  ground-state atoms by resonance light from a  $^{200}\text{Hg}$  lamp. Appendix B presents a detailed calculation which gives the total energy shift of each isotope in terms of a single dispersion integral, which we represent below [cf. Eq. (4.6)] by a parameter  $c$ , to be determined experimentally. Note that the  $^{200}\text{Hg}$  resonance light is several Doppler widths away from any  $^{199}\text{Hg}$  or  $^{201}\text{Hg}$  transitions (see Table VI) so it does not produce any optical pumping or real light shifts.

The light-shift calibration arrangement is shown in Fig. 3. Before the  $^{200}\text{Hg}$  light enters the oscillator cell, it passed through a 2.5-cm-long absorption cell which contains a droplet of  $^{201}\text{Hg}$ . The vapor pressure of Hg gives about ten absorption lengths for the  $^{201}\text{Hg}$  resonance light over the length of the cell. The purpose of the filter cell is to absorb any light from impurity Hg isotopes (about 5%) in the  $^{200}\text{Hg}$  lamp which could optically pump the  $^{201}\text{Hg}$  and the  $^{199}\text{Hg}$  (the  $^{201}\text{Hg}$  and  $^{199}\text{Hg}$  transitions are close enough so that  $^{201}\text{Hg}$  is an effective filter for both isotopes). The light that passed through the filter cell is collimated by a 4-in.-diam Suprasil fused-silica lens. The collimated light is then linearly polarized by passing it through a Polacoat UV-105 ultraviolet po-

larizing filter with its polarization axis at an angle  $\phi$  relative to  $\hat{x}_c$ . The light is then passed through a quartz-compression quarter-wave plate (identical to that described in Sec. III F) with its slow axis at an angle  $\alpha$  relative to  $\hat{x}_c$ . There are holes in the magnetic shields and field coils, and a fused-silica window in the oven, through which the light passes; the light irradiates the atoms in the optical-pumping cell causing the energy shifts of interest. For stability, the calibration lamp is kept on constantly during an experiment that requires calibration. Between calibration runs the calibration light is blocked with a shutter.

In the calibration frame we can readily work out the light polarization as a function of  $\alpha$  and  $\phi$ . The polarization vector is

$$\hat{e} = \hat{x}_c \cos\phi + \hat{y}_c \sin\phi ,$$

Let  $\hat{\alpha}$  be a vector parallel to the slow axis of the quarter-wave plate,

$$\hat{\alpha} = \hat{x}_c \cos\alpha + \hat{y}_c \sin\alpha .$$

The component of  $\hat{e}$  parallel to  $\hat{\alpha}$  gets multiplied by  $e^{i\delta}$  with  $\delta = -\pi/2$  if the quarter-wave plate is perfect (we will consider imperfectly polarized light later), while the component perpendicular to  $\hat{\alpha}$  is unaffected. Thus, the light polarization becomes

$$\begin{aligned} \hat{e}' &= [\hat{e} \cdot \hat{\alpha}] \hat{\alpha} e^{i\delta} + \hat{e} - [\hat{e} \cdot \hat{\alpha}] \hat{\alpha} \\ &= [e^{i\delta} \cos(\phi - \alpha) \cos\alpha + \sin(\alpha - \phi) \sin\alpha] \hat{x}_c \\ &\quad + [e^{i\delta} \cos(\phi - \alpha) \sin\alpha + \sin(\phi - \alpha) \cos\alpha] \hat{y}_c . \end{aligned}$$

In the spherical basis (see Appendix B) the light polarization is

$$e_{\pm} = \mp (e'_x \mp i e'_y) / \sqrt{2}, \quad e_0 = 0 .$$

We now need to transform the polarization vector to the experiment frame. Referring to Fig. 3,

$$\hat{e}_E = d_{y_E}^1(-\beta) d_{z_L}^1(45^\circ) d_{y_L}^1(-90^\circ) \hat{e}_c .$$

(See Refs. 19 and 20 for the rotation matrices.) Note that the relationship between the  $xyz$  frame of Fig. 2 and the  $L$  and  $E$  frames is spelled out in the caption to Fig. 3. Table I lists values of  $e_d = e_+^2 - e_-^2$  and  $e_q = 1 - 3e_0^2$ , the dipole and quadrupole components of the light polarization in the experiment frame, for various values of  $\alpha$ ,  $\beta$  and  $\phi$ , with  $\delta = -\pi/2$ .

The quadrupole calibration is carried out as follows.  $\beta$  is set by the current experimental conditions;  $\alpha$  is set to either  $90^\circ$  or  $45^\circ$  (gives a larger quadrupole shift) and remains at that angle throughout the calibration.  $\phi$  is then increased from  $0^\circ$  to  $135^\circ$  in steps of  $45^\circ$ , then back to  $0^\circ$  in one step. At each value of  $\phi$  we wait for the system to stabilize and then measure the change in  $V_{\text{out}}^{201}$  and  $V_{\text{corr}}$  that results from the light shifts.

Using Eqs. (4.1), (4.2), (B2), and (B3), we find that the energy shifts are

TABLE I. Dipole and quadrupole components of the calibration light in the experimental frame.

$\alpha$	$\phi$	$\beta$	$e_d$	$e_q$
90.0	0.0	-45.0	0.000	-0.500
90.0	45.0	-45.0	-0.500	-0.125
90.0	90.0	-45.0	0.000	0.250
90.0	135.0	-45.0	0.500	-0.125
90.0	0.0	-135.0	0.000	-0.500
90.0	45.0	-135.0	-0.500	-0.125
90.0	90.0	-135.0	0.000	0.250
90.0	135.0	-135.0	0.500	-0.125
45.0	0.0	-45.0	-0.500	-0.125
45.0	45.0	-45.0	0.000	-1.186
45.0	90.0	-45.0	0.500	-0.125
45.0	135.0	-45.0	0.000	0.936
45.0	0.0	-135.0	-0.500	-0.125
45.0	45.0	-135.0	0.000	0.936
45.0	90.0	-135.0	0.500	-0.125
45.0	135.0	-135.0	0.000	-1.186

$$E_d = c \left[ -\frac{0.485}{\sqrt{5}} e_d \right] ,$$

$$E_q = c(0.122 e_q) , \quad (4.6)$$

$$E'_d = c(0.339\sqrt{2} e_d) ,$$

where  $c$  is a constant to be determined. In terms of measured voltages,

$$\xi V_{\text{out}}^{201} = \gamma_{201} \delta B + E_d + \eta E_q + V_0 ,$$

$$\delta B = \alpha_m \Delta V_{\text{corr}} / \sqrt{2} ,$$

where  $V_0$  is a constant offset which we ignore, and  $\delta B$  is the correction field automatically applied to compensate for the dipole light shift  $E'_d$  of  $^{199}\text{Hg}$ . Thus

$$\xi V_{\text{out}}^{201} = \gamma_{201} \delta B + c(-0.217 e_d + 0.122 \eta e_q) , \quad (4.7)$$

$$\delta B = c(0.479 e_d) / \gamma_{199} . \quad (4.8)$$

We could combine these equations which would make the measurement of  $\delta B$  unnecessary; however, there is a unfortunate near cancellation

$$\frac{\gamma_{201}}{\gamma_{199}} (0.479) - 0.217 = -0.40 .$$

Since the dispersion overlap integrals are only about 10% accurate, the  $-0.040$  has an uncertainty of about 50%.

From the values of  $e_d$  and  $e_q$  given in Table I we can see that for  $\alpha = 90^\circ$ ,  $V_{\text{out}}(\phi = 0^\circ) - V_{\text{out}}(90^\circ)$  will contain only the quadrupole component of the light shift while  $V_{\text{out}}(45^\circ) - V_{\text{out}}(135^\circ)$  will contain only the dipole component (the reverse for  $\alpha = 45^\circ$ ). Thus,  $\eta$  is readily determined. Table II gives  $\beta, \alpha$ , the experimental measurements,  $\xi, \eta$ , and  $c$  for some calibration runs.  $c$  was determined by Eq. (4.7). As a check  $c$  was also determined from Eq. (4.8), listed as  $c'$  in Table II (b). The uncertainty in  $\Delta V_{\text{corr}}$  is about 10 bits; in all other measurements the uncertainty is 2 bits. The units of  $\xi$  are  $\mu\text{Hz/bit}$  and

TABLE II. Results of the light-shift calibrations. Values in parentheses denote uncertainties.

Run	(a) Raw data (the uncertainty in the $V_{\text{out}}$ is $\pm 2$ bits)							
	$\phi=0$		$\phi=45^\circ$		$\phi=90^\circ$		$\phi=135^\circ$	
	$V_{\text{out}}$	$V_{\text{corr}}$	$V_{\text{out}}$	$V_{\text{corr}}$	$V_{\text{out}}$	$V_{\text{corr}}$	$V_{\text{out}}$	$V_{\text{corr}}$
1	-92	0(8)	-41	-50(8)	41	0(8)	45	50(8)
2	-78	0(8)	-67	-48(8)	21	0(8)	-4	48(8)
3	24	0(6)	1	-49(6)	-11	0(6)	17	49(6)
4	40	-21(7)	85	0(7)	-20	21(7)	-81	0(7)
5	78	-25(5)	106	0(5)	-91	25(5)	-104	0(5)
6	74	-27(7)	98	0(8)	-90	27(7)	-106	0(7)
7	53	-28(6)	83	0(6)	33	28(6)	-72	0(6)
8	53	-25(10)	89	0(10)	-33	25(10)	-80	0(10)

Run	(b) Combined theory and experiment; determinations of $c$ and $\eta$						
	$\alpha$	$\beta$	$\xi$	$c$	$\eta c$	$\eta$	$c'$
1	90	-135	+2.45(0.05)	3435(500)	3561(1187)	1.04(0.38)	5400(611)
2	90	-135	+3.21(0.05)	3297(500)	3473(1187)	1.05(0.39)	5184(611)
3	90	-45	+3.49(0.05)	4060(377)	-1335(893)	-0.33(0.22)	5292(458)
4	45	-45	+4.69(0.05)	3147(441)	-3007(371)	-0.96(0.18)	2268(535)
5	45	-135	+2.83(0.05)	4407(316)	2296(266)	0.52(0.07)	2700(382)
6	45	-135	+2.84(0.05)	4525(439)	2238(396)	0.49(0.10)	2916(535)
7	45	-45	+3.49(0.05)	2789(377)	-2090(317)	-0.75(0.15)	3024(458)
8	45	-45	+3.21(0.05)	3475(625)	-2095(524)	-0.60(0.19)	2700(764)

the units of  $c$  and  $c'$  are  $\mu\text{Hz}$ . Note that  $c$  and  $c'$  are in fairly good agreement. The fluctuations in  $c$  include drifts in the calibration-lamp intensity and spectral characteristics.

We will now describe the checks we performed on several possible systematic effects which could affect the calibration. First, we determined the range of uncertainty (offsets) of the angles  $\delta$ ,  $\phi$ , and  $\alpha$ , and determined that they could not affect the calibrations significantly. In determining the dipole sensitivity, we changed  $f$  by both  $+120$  and  $-120 \mu\text{Hz}$  and verified that the output voltage changed linearly.

Another possible systematic could occur from the small amount of pumping which the calibration light causes due to impurity isotopes in the enriched  $^{200}\text{Hg}$  lamp. The filter cell does not completely absorb all light which is resonant with the  $^{201}\text{Hg}$  and the  $^{199}\text{Hg}$  contained in the optical-pumping cell. This is because the filter cell is at room temperature (300 K) and has a Doppler width more narrow than the atoms in the optical pumping cell (573 K), and the lamp width is greater than either (about 1000 K). The in-phase amplitude of each oscillator is reduced by about 10% when the calibration light is admitted into the pump cell, and as the calibration-light polarization is varied, there is a 5% variation in the in-phase amplitudes. This is because different polarizations pump differently. We did a measurement to see if the light-induced energy shifts were linear with the calibration-light intensity ( $I$ ) by doing calibrations at  $I_0$  and  $0.6I_0$ . The shifts were linear to within the experimental uncertainties. The decrease in the in-phase amplitudes was approximately quadratic in  $I$ .

We also did a calibration run without the filter cell. Without the filter cell the in-phase amplitudes were re-

duced by over a factor 2. This is explained by the presence of impurity isotopes which cause optical pumping. A mass spectrometer was used to measure the isotopic abundances of the various Hg isotopes in the enriched  $^{200}\text{Hg}$  used to make the lamp. We found that there was indeed a 5% concentration of isotopes which could cause optical pumping. Since the calibration-lamp intensity is about ten times that of the pump lamp, we expect a 50% increase in the light-induced relaxation rate (the calibration-lamp impurities probably do not contribute to the creation of polarization but only cause light-induced relaxation). Because the in-phase amplitudes vary inversely as the relaxation rate squared ( $\Gamma_R^{-2}$ ), the 50% increase in  $\Gamma_R$  would change the in-phase amplitudes by a factor of  $1/(1+0.5)^2=0.44$ , very close to what we observed. With the filter cell still removed, we then decreased the calibration-light intensity by a factor of 10 with a neutral density filter and repeated the calibration. Compared to the measurements using the filter cell, there was a 10% decrease in the in-phase amplitudes, as expected [ $1/(1+0.05)^2=0.91$ ]. However, the results of the calibration showed energy shifts  $\frac{1}{5}$  of those with just the filter cell in place; one would expect the shifts to be  $\frac{1}{10}$  as large. By mass spectroscopic analysis it was determined that there was a small amount of  $^{200}\text{Hg}$  in the enriched  $^{201}\text{Hg}$  used to make the filter cell. The concentration was enough to reduce the transmitted  $^{200}\text{Hg}$  resonance light by a factor of 2. We verified this factor of 2 experimentally by measuring the intensity of the transmitted resonance light with the sidearm of the filter cell cooled to liquid-nitrogen temperature (no Hg in the cell) and then at room temperature. By these measurements we determined that the filter cell cuts down the light resonant with  $^{199}\text{Hg}$  and  $^{201}\text{Hg}$  by a factor of 10.

Note that any distortion of the resonance line shape of the  $^{200}\text{Hg}$  due to the absorption in the filter cell will have very little effect on the dispersion integral since the dispersion function is slowly varying away from line center.

Finally, we verified that none of the calibration light scattered by the atoms in the optical-pumping cell gave a precession signal which could result in a false phase shift. There was no change in the dc voltage from the detection photomultiplier as the calibration light was turned on and off. Also no precession signal was observed when the pump light was turned off and the calibration light turned on. The solid angle subtended by the light pipe was 0.35 sr; the calibration-lamp-impurity light intensity was 5% of the pump lamp intensity. Thus the maximum possible precession signal amplitude from the calibration-lamp impurities would be  $0.05 \times (0.35/4\pi) = 4 \times 10^{-4}$  which is negligible.

In addition to the virtual light shift, there can be a "real" light shift.<sup>4</sup> This shift arises because when being pumped, the atoms spend some fraction of time in the excited state where the atomic magnetic moment is different. We can estimate the effect:

$$2\pi\delta\nu \approx \Gamma_p \gamma_e B \tau,$$

where  $\Gamma_p \approx 0.01$  sec is the pump rate (from the pump lamp),  $B \approx 20$  mG is the static magnetic field strength,  $\gamma_e/2\pi \approx 700$  Hz/mG is the excited-state gyromagnetic ratio (actually, the difference between the ground-state and excited-state gyromagnetic ratios), and  $\tau = 120$  nsec is the excited-state lifetime. For the (204) pump lamp,  $\delta\nu = 4$   $\mu\text{Hz}$ . Since the pump rate of the calibration lamp is much smaller than that of the pump lamp, the calibration lamp real-light shift will be  $< 1$   $\mu\text{Hz}$ , about a factor of 500 less than the virtual-light shift.

In view of these tests and the agreement among the values of  $c$  in Table II(b), we are confident of the validity of the light-shift calibration.

### C. Measurement of $Q/\mathcal{D}$ and estimating $\eta$ using the free-precession calculation

We also estimated  $\eta$  by measuring  $Q/\mathcal{D}$  and using Eq. (2.7)

$$\eta \approx \frac{\delta\omega_Q}{\omega_Q}. \quad (4.9)$$

$Q/\mathcal{D}$  was measured as follows. The atomic-oscillator light-modulation amplitude was measured. The rf ( $B_y$ ) field was turned off and the pump-light quarter-wave plate was simultaneously set to  $0^\circ$  so that the incident light was linearly polarized along  $\hat{y}_L$ , and the light modulation amplitude was measured. We converted the 5.5-Hz modulation to about 0.1 Hz by heterodyning with a reference oscillator near 5.5 Hz through a lock-in amplifier. Since all of the measurements were made from the heterodyned signal which preserves phase information, we could, in addition to measuring the decrease of the modulation amplitude, measure the phase change relative to the reference oscillator (it would be difficult to

measure the phase shift at 5.5 Hz directly). The amplitude decreased by a factor of  $0.08 \pm 0.03$ , and the phase changed by  $50 \pm 15^\circ$ .

In the experiment frame for light polarized along  $\hat{y}_L$  (see Fig. 3)

$$\text{Re}(e_+^* e_0 - e_0^* e_-) = -\frac{\sqrt{2}}{2} \sin\beta \cos\beta,$$

and

$$\text{Im}(e_+^* e_0 - e_0^* e_-) = \frac{\sqrt{2}}{2} \sin\beta.$$

Also,

$$e_+^* e_0 + e_0^* e_- = 0.$$

Inserting this into Eq. (2.4) ( $\theta = \beta = -45^\circ$ ), we find for the phase shift  $\phi$ ,

$$\tan\phi = -\frac{\text{Im}(e_+^* e_0 - e_0^* e_-)}{\text{Re}(e_+^* e_0 - e_0^* e_-)} = \frac{1}{\cos\beta}, \quad \phi = 55^\circ$$

in agreement with the measured value and, for plane-polarized light,

$$(\Delta I)_{\text{PP}} = \sqrt{3} Q/40. \quad (4.10)$$

For circularly polarized light in the lab frame at  $\beta = 45^\circ$  from Eq. (2.4) we find

$$(\Delta I)_{\text{CP}} = \frac{\sqrt{5}}{20} \mathcal{D} + \frac{1}{40} Q. \quad (4.11)$$

Thus, taking the ratio of Eqs. (4.10) and (4.11) we find that  $Q/\mathcal{D}$  is  $0.22 \pm 0.08$ . Using Eqs. (2.1) and (4.9), we find that  $|\eta| = 0.33 \pm 0.07$ , in agreement with calibration 6 ( $\eta = 0.49 \pm 0.10$ ) which was carried out under the same conditions.

In retrospect, this method of determining  $\eta$  is relatively simple and could have received more emphasis. Note, however, that we had to assume in Eq. (2.7) that the octupole polarization  $\mathcal{O}$  is small enough not to have a major effect on the sensitivity.

We can also compute  $\xi$ , the dipole calibration factor defined in Eq. (4.4),

$$\begin{aligned} \xi &\approx \frac{\pi}{T} V_{\text{in}}^{-1} = 1/(1600 \text{ bit} \times 85 \text{ sec} \times \pi) \\ &= 2.34 \text{ } \mu\text{Hz/bit}, \end{aligned}$$

in good agreement with the observed value.

### D. Numerical solution to the spin- $\frac{3}{2}$ atomic oscillator

We have also solved the Bloch equations with optical pumping for the spin- $\frac{3}{2}$  atomic oscillator. We followed the formalism developed in Ref. 4 and solve for the density matrix in the rotating frame with the assumption that all of the multipole moments decay at the same rate and we only account for the diagonal components of repopulation pumping. We determine the phase of the transmitted light relative to the oscillating field as a function of quadrupole and dipole energy shifts. The result of a nu-

merical calculation of  $\eta$  gives  $0.2 < \eta < 0.6$ , where the range of  $\eta$  is set by the uncertainty in the experimental conditions. The measured values of  $\eta$  fall roughly within this range.

## V. OBSERVATION OF WALL RELAXATION AND WALL SHIFTS

Interaction between the atoms and the inner surface of the fused-silica cell (bottle) results in relaxation of the density-matrix multipoles and in energy shifts among the Zeeman levels. The energies associated with these interactions are small compared to the Larmor frequencies and can be considered as perturbations. The perturbations can arise from impurities stuck on or in the fused silica (paramagnetic, ferromagnetic, or electrostatic in character), surface strains in the fused silica (possibly electrostatic), or by a weak fluctuating perturbation which is a property of the fused-silica surface. The cause of the perturbation is, in general, unknown. A major study of relatively large wall shifts by optical pumping has been published recently.<sup>6</sup>

### A. Relaxation due to a weak fluctuating isotropic perturbation

The relaxation rate for each multipole moment  $L$  of an atomic ensemble due to an isotropic perturbation of multipolarity  $l$  is given by<sup>21</sup>

$$\gamma_L(l) = 2v^2\tau_c[(2K+1)^{-1} - W(LKKl, KK)] , \quad (5.1)$$

where  $W$  is the Racah coefficient (couples three angular momenta),  $K$  is the spin of the atoms,  $\tau_c$  is the perturbation correlation time, and  $v^2$  is the magnitude of the perturbation. The relaxation rate is independent of  $M$  (isotropic) when the applied magnetic field is weak ( $\omega_L\tau_c \ll 1$ , where  $\omega_L$  is the Larmor frequency). This condition applies throughout our measurements.

The atoms are subjected to the perturbation only while they are stuck on the cell wall. According to the theory of physical adsorption<sup>22</sup> the average dwell time for an atom on the wall is

$$\tau_s = \tau_0 \exp(E_a/kT) , \quad (5.2)$$

where  $E_a$  ( $\approx 0.1$  eV) is the binding energy of the atom to the surface and  $T$  is absolute temperature. The constant  $\tau_0$  ( $\approx 10^{-12}$  sec) is a time on the order of the vibrational period of the atom on the surface.<sup>4</sup>

When an atom breaks loose from the wall it travels through the cell undisturbed (no buffer gas, atomic vapor density is low) until it is again adsorbed on the wall. The time of flight from wall to wall is

$$\tau_v = l/v \approx 5 \times 10^{-5} \text{ sec} , \quad (5.3)$$

where  $l$  is a characteristic linear dimension of the cell and  $v$  is the mean velocity of the atom. Thus, one would expect that the relaxation rate is reduced by the fractional time that the perturbation occurs,

$$\gamma_L(l) = \frac{\tau_s}{\tau_s + \tau_v} \gamma_L(l) , \quad (5.4)$$

since the perturbation only occurs during the time  $\tau_s$ . All experimental evidence indicates that  $\tau_s \ll \tau_v$ .<sup>4,23,24</sup>

The relaxation rates were measured by "pumping" the atoms with polarized light for many lifetimes (the lifetime  $T = 1/\gamma$ ) with a small magnetic field (15 mG) parallel to the light beam. The field is then suddenly rotated by  $45^\circ$ , and the free precession of the multipoles is observed as a modulation of the transmitted pumping light. The signal from  $^{199}\text{Hg}$  is a simple exponentially decaying sinusoid, while the  $^{201}\text{Hg}$  signal is a sinusoid with a time-dependent amplitude which must be described by several exponential decay constants and possible quadrupole perturbations.  $Q$  and  $\mathcal{D}$  become functions of time;

$$Q(t) = Q_0 \exp(-\gamma_2 t) ,$$

$$\mathcal{D}(t) = \mathcal{D}_0 \exp(-\gamma_1 t) ,$$

where  $\gamma_L = \sum_l \gamma_L(l)$ , the sum extending over all perturbations which cause relaxation, which in general includes the light. The octupole does not cause a modulation of the transmitted light and is not directly observable.

In our measurements, we consider only the  $1\omega$  terms of Eq. (2.7); in terms of the transmitted intensity,

$$I^{199}(t) = I_0^{199} \exp(-\gamma' t) \sin(\omega t) ,$$

$$I^{201}(t) = I_0^{201} [A(t) \cos(\omega t) + B(t) \sin(\omega t)] ,$$

where  $A(t)$  and  $B(t)$  are determined from Eq. (2.4) and the time dependence of  $Q$ ,  $\mathcal{D}$  given above. The total relaxation rate is given by

$$\gamma_L^{\text{tot}}(l) = \gamma_L^{\text{light}}(l) + \gamma_L(l) .$$

Thus, to measure  $\gamma_L(l)$  we must either let the atoms evolve in the dark and take before and after measurements or we can measure  $\gamma_L^{\text{tot}}(l)$  for several light intensities and extrapolate to zero intensity.

During the free-precession measurements the atoms precess at their respective Larmor frequencies; the magnitude of the field is such that  $f_{199} = 15$  Hz and  $f_{201} = 5.5$  Hz. The modulation on the light is heterodyned to a lower frequency using a lock-in amplifier referenced to an oscillator set near the Larmor frequency of interest (0.25 Hz away). The time constant of the lock-in is set to readily pass the frequency difference signal ( $\tau = 1$  sec), while the sum-frequency signal is highly attenuated. Converting the signal to lower frequency serves two purposes: the  $^{201}\text{Hg}$  and  $^{199}\text{Hg}$  modulations can be separated, and the resulting 0.25 Hz is readily recorded with a strip-chart recorder.

The  $^{199}\text{Hg}$  lifetime was measured using circularly polarized light. After the field was rotated the amplitude of the precession signal was measured ( $I_1$ ). The light beam was then blocked for a time  $\Delta t$ , after which it was unblocked and the precession amplitude again measured ( $I_2$ ). The lifetime is given by

$$\tau = 1/\gamma_1 = \Delta t / \ln(I_1/I_2) .$$

Under normal operating conditions,  $\tau = 1200 \pm 100$  sec. The light intensity was typically set so that  $\tau_{\text{tot}} = 1/\gamma_{1,\text{tot}} = 80$  sec. The relaxation rate including the light-induced relaxation is readily determined; the free-precession decay is recorded in its entirety and the decay

rate is determined from this recording.

The  $^{201}\text{Hg}$  free-precession signal was measured at two different light intensities as shown in Fig. 4. Note that there is clearly a nonexponential decay. The envelope of the  $^{201}\text{Hg}$  signal is given by

$$I(t) = I_0 [A^2(t) + B^2(t)]^{1/2},$$

where we have assumed that the rate of change of the amplitude is much less than 0.25 Hz (note that the lock-in preserves relative phase). The light-induced quadrupole shift accounts for most of the nonexponential character. A nonlinear least-squares fit to  $Q$ ,  $\mathcal{D}$ ,  $\omega_Q$ ,  $I_0$ , and  $\gamma_2(2) = 2\gamma_1(2)$  (the form of the relaxation will be described later) gives an  $\omega_Q$  of 3 mHz for  $I_0$  and 1.5 mHz for  $0.36 I_0$ . Extrapolating to zero light intensity gives  $\omega_Q = 700 \pm 700 \mu\text{Hz}$ .

With reduced light intensity this light shift is reduced, and the decay envelope (with circularly polarized pump light) is determined mostly by  $\mathcal{D}$ . The free-precession decay is recorded for two light intensities, and the decay rate is extrapolated to zero intensity;  $\gamma_1$  is thus determined. This procedure is repeated using linearly polarized pump light. In this case, the decay envelope is determined mostly by  $Q$ . The result of the two decay rates give  $\gamma_2 = (2.0 \pm 0.1)\gamma_1$  over a wide range of conditions. This is consistent with the relaxation being caused by a quadrupole interaction between the  $^{201}\text{Hg}$  ( $I = \frac{3}{2}$ ) nuclear quadrupole moment and electric field gradients present on the cell wall [Eq. (5.1)]. We can rule out magnetic dipole relaxation as the dominant relaxation mechanism since this would require  $\gamma_2(1) = 3\gamma_1(1)$  and a much faster  $^{199}\text{Hg}$  relaxation rate. The relaxation of the  $^{201}\text{Hg}$  being due primarily to a quadrupole interaction is consistent with previous experimental work.<sup>25,26</sup>

Under normal operating conditions of the apparatus,  $(\gamma_2/2)^{-1} = (\gamma_1)^{-1} = 80 \pm 5$  sec, and the light intensity was set so that  $(\gamma_1^{\text{tot}})^{-1} = 50 \pm 5$  sec. A least-squares fit to the decay signal gives  $\omega_Q = 0 \pm 300 \mu\text{Hz}$ , independent of light intensity. With our signal-to-noise ratio and lifetimes,

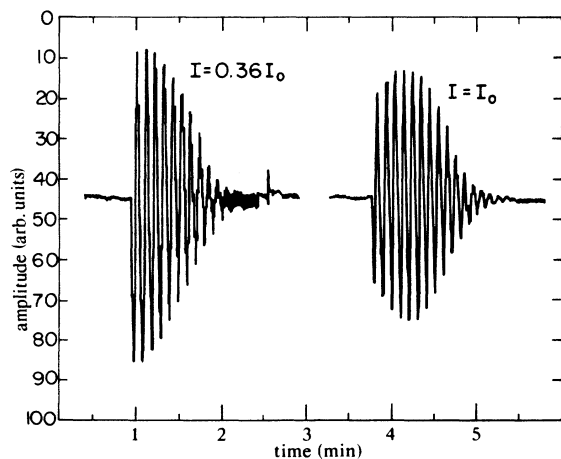


FIG. 4. Examples of nonexponential decay in the spin- $\frac{3}{2}$   $^{201}\text{Hg}$  system.

about 1 mHz is the minimum resolvable quadrupole shift from measurements of the free-precession envelope.

### B. Temperature dependence of the relaxation rate

We also measured how the in-phase amplitude of the atomic oscillator varied with temperature under the operating conditions of the anisotropy experiment. The relaxation rates, according to Eqs. (5.2) and (5.3), should depend on temperature as

$$\gamma \propto T^{1/2} \exp(E_a/kT),$$

where  $\tau_v \propto T^{-1/2}$  and  $\tau_s \propto \exp(E_a/kT)$ ,  $\tau_s \ll \tau_v$ . The in-phase amplitude of the  $^{199}\text{Hg}$  atomic oscillator is given by (see Appendix A)

$$I \propto \frac{\omega_1 \Gamma_p}{(\Gamma_p + \gamma)^2 + \Delta\omega^2 + \omega_1^2},$$

where  $\Gamma_p$  is the pump-light intensity,  $\gamma$  is the relaxation rate,  $\Delta\omega$  is the frequency offset (zero under operating conditions), and  $\omega_1$  is the RF field amplitude. When the temperature is varied, only  $\gamma$  should be affected. This equation is approximately true for the  $^{201}\text{Hg}$  atomic oscillator.

We measured the in-phase amplitude of each atomic oscillator at several temperatures between 500 and 600 K and fit the experimental data to the function

$$I(t) = \frac{a_1}{[a_2 + \exp(a_3/T)T^{1/2}]^2 + a_4^2}.$$

The fits give  $a_3 = 3335(1)$  K for the  $^{199}\text{Hg}$  and  $a_3 = 4494(2)$  K for the  $^{201}\text{Hg}$ . The experimental data and the least-squares fit for each is plotted in Fig. 5. These

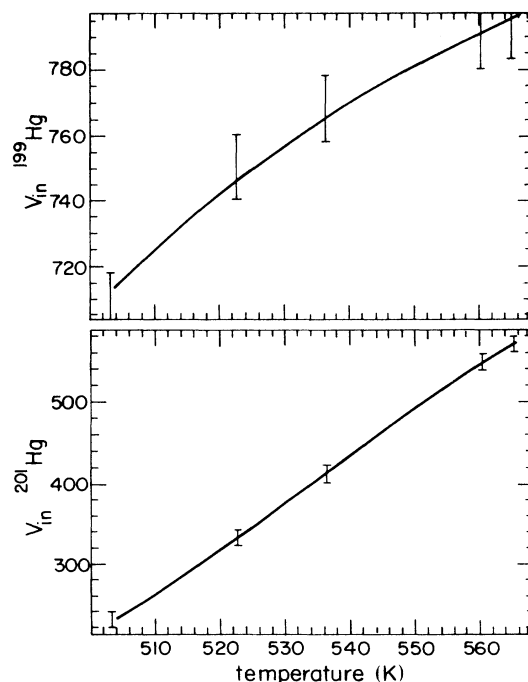


FIG. 5. In-phase amplitudes vs cell temperature.

amplitudes agree with the results expected given the known pump and relaxation rates. The relative sizes of the RF amplitudes are also in good agreement with the operating conditions.

### C. Measurement of the bottle shift

It is also of interest to measure the “frozen-in” quadrupole moment of the cell which leads to a quadrupole energy shift (bottle shift) among the Zeeman levels. In weak magnetic field the perturbation which causes the relaxation also causes small energy shifts.<sup>21</sup> If the perturbation has a nonzero average over a small area (possibly because the surface electric field induced by an atom always points in the same direction), and if this average is the same for every small area of the cell surface, there can be a net quadrupole moment in the cell if the cell has a symmetry such that  $Y_{LM}(\theta, \phi)$  is nonzero when averaged over the surface for some  $L$  and  $M$ .<sup>26</sup> Another likely source of a quadrupole moment is a surface imperfection (strain in the fused silica, a speck of dirt) that creates an electric field gradient of arbitrary magnitude and direction at a specific point in the cell.

It should be emphasized that it is possible to make cells shaped so as to greatly enhance the quadrupole bottle shift. Instead, what we do here is to use the high sensitivity of our technique to measure the residual quadrupole moment of the nearly spherical cell.

We measured the quadrupole moment of the cell directly by rotating it. The oven was equipped with a mechanical means of rotating the cell without affecting the atomic oscillators in any other way (cell temperature, magnetic field, etc. held constant). Figure 6 shows the coordinate system used to describe the rotation of the cell. The cell is rotated about an axis  $5^\circ$  away from the stem axis.  $\phi$  is incremented in steps of  $45^\circ$  from  $0^\circ$  to  $360^\circ$  ( $\phi$  is the azimuthal angle which gives the angle through which the cell has been rotated). At each  $\phi$ , the system is allowed to stabilize (10 min) and the out-of-phase volt-

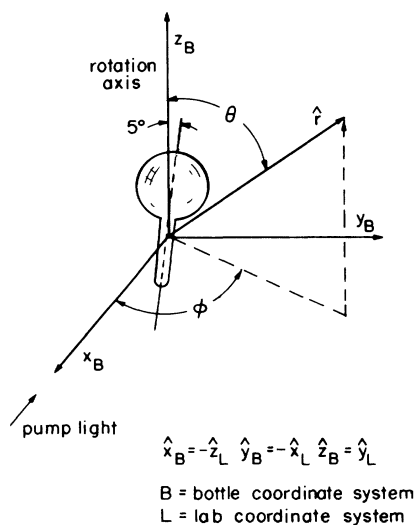


FIG. 6. Coordinate system used to describe rotation of the cell.

ages, in-phase voltages, and magnetic-field-correction signal are measured. The measurements were done for two magnetic field configurations. The system was calibrated at each field configuration.

Our data turn out to be consistent with a quadrupole bottle shift having a single axis of symmetry. For such a case, as in Eq. (2.2), the frequency shift of the atomic oscillator will depend on  $P_2(\cos\alpha)$  where  $\alpha$  is the angle between the quadrupole axis  $\hat{r}_Q$  and the magnetic field axis  $\hat{r}_m$  (the quantization axis). We write

$$\begin{aligned} \cos\alpha &= \hat{r}_Q \cdot \hat{r}_m \\ &= \cos\theta_Q \cos\theta_m + \sin\theta_Q \sin\theta_m \cos(\phi + \phi_Q - \phi_m), \end{aligned}$$

where  $\phi$  is the azimuth of a reference point fixed in the cell and  $\phi_Q$  is the azimuth of  $\hat{r}_Q$  relative to this reference point. The complete expression we use is

$$E = E_Q P_2(\cos\alpha) + E_0,$$

where  $E_0$  accounts for any instrumental offset for the set of measurements. When the cell is rotated,  $\phi$  is varied.  $\theta_m$  and  $\phi_m$  are set by the magnetic field configuration, leaving  $E_Q$ ,  $E_0$ ,  $\phi_Q$ , and  $\theta_Q$  to be determined. A nonlinear least-squares fit to the data was used to determine these parameters from the experimental data. Figure 7 shows the quadrupole calibrated raw data and the fit. Figure 8 is a polar plot of the raw data minus  $E_0$  and of  $E_Q P_2(\cos\alpha)$  using the fit parameters. The fit coefficients are listed in Table III.

The quadrupole calibration changed sign with the field flip; the raw data on the field minus run was “upside down,” as expected. The field change is equivalent to ro-

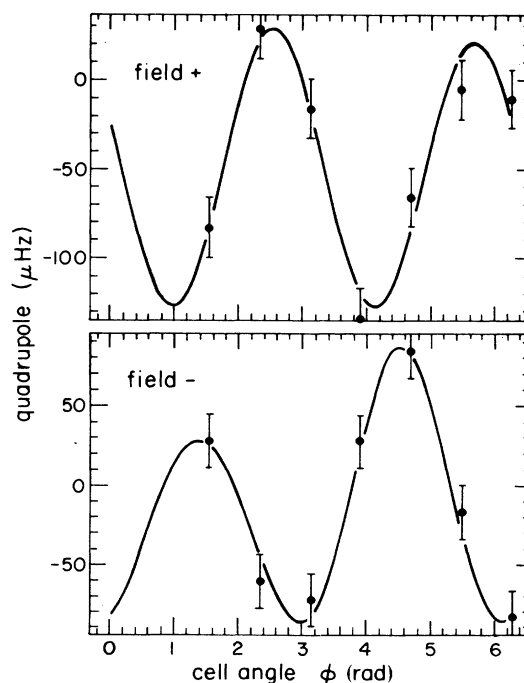


FIG. 7. Bottleshift data and least-squares fit.

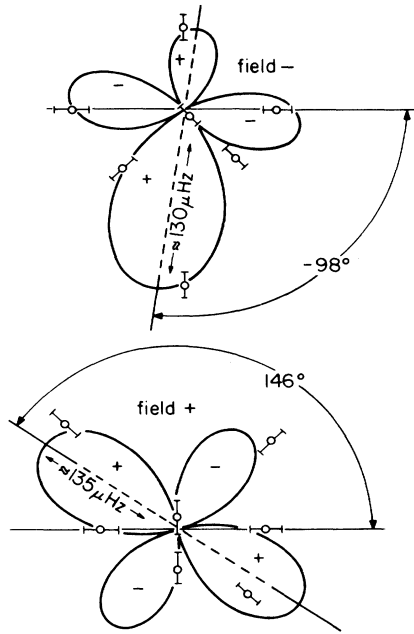


FIG. 8 Polar plot of the bottleshift data.

tating the cell by  $\phi_m^+ - \phi_m^-$ . Note that the change in the symmetry axis of the graphs in Fig. 8 is almost exactly  $\phi_m^+ - \phi_m^-$ . Note also that the fit angles and quadrupole magnitudes as determined with each field configuration (Table III) agree within experimental error.

To fully parametrize the quadrupole interaction we would have to expand the angular dependence of the shift in terms of the spherical harmonics  $Y_{lm}(\theta, \phi)$ . Since we were able to rotate about only one axis, such an expansion for our data would be unreliable. However, the assumed axially symmetric form of the cell quadrupole parametrizes the angular dependence to within the experimental uncertainties.

Although the agreement between the assumed form of the quadrupole energy shift and the data is excellent, there are some possible systematic effects which could have been a problem. Focussing effects of the light by the cell could result in changes in the light-induced energy shift, possibly mimicking a quadrupole. Also, changes in the optical pumping could cause changes in the calibration which result in apparent energy shifts as the cell is rotated. However, the changes in the in-phase amplitudes and the magnetic field correction signal were small enough to rule out these effects (a change in the light shift would show up in the correction signal; a change in pumping characteristics would show up in the in-phase signals).

These measurements indicate that the quadrupole symmetry axis is almost perpendicular to the stem axis. However this set of measurements is relatively insensitive to a quadrupole symmetric along the bottle stem axis which is nearly coincident with the axis of rotation. Other measurements, described next, indicate that any such stem-symmetric quadrupole must be very small.

We measured how the quadrupole shift varied with temperature. If we assume that  $E_Q$  has the same functional form as the relaxation rate

$$E_Q = E'_0 e^{E_a/kT} T^{1/2},$$

we find that

$$\frac{\partial E_Q}{\partial T} = \frac{E_Q}{T} \left[ \frac{1}{2} - \frac{E_a}{kT} \right].$$

We set the cell angle to the maximum quadrupole shift (as determined by the rotation data; see Fig. 8, field minus) and changed the temperature by about  $\pm 15$  K. We then repeated this set of measurements with the cell rotated by  $90^\circ$ . We expected that this rotation would change the contribution to  $\partial E/\partial T$  from the measured bottle quadrupole to  $-\frac{1}{2}$  its value, while the contribution from a possible bottle quadrupole symmetric about the stem would remain essentially the same. We found that

$$\left. \frac{\partial E}{\partial T} \right|_0 = -2.3 \pm 0.2 \mu \text{ Hz/K},$$

$$\left. \frac{\partial E}{\partial T} \right|_{90} = +1.1 \pm 0.2 \mu \text{ Hz/K}$$

at 537 K. This demonstrates that any stem quadrupole is small compared to the quadrupole which rotates with the cell. Inserting the values given above and  $E_Q \approx 135 \mu\text{Hz}$ , we find  $E_a = 4600 \pm 400$  K, in good agreement with the previous determination of  $E_a$ .

This rules out (for this cell) the possibility that the bottle shift is dominated by a homogeneous surface quadrupole interaction which does not average to zero because of lack of sufficient cell symmetry. If this were the origin of the bottle shift the quadrupole should have its symmetry axis along the stem as this is the largest deviation from spherical symmetry in the cell. It is more likely that the bottle shift arises from surface imperfections on the cell walls which create a nonzero average electric field gradient for atoms adsorbed on the walls. This is also consistent with the fact that the temperature dependence of the  $^{201}\text{Hg}$  relaxation rate indicates a stronger surface binding energy than for the  $^{199}\text{Hg}$ . Since an electric quadrupole perturbation will not affect the  $^{199}\text{Hg}$ , its relaxation rate is presumably dominated by magnetic dipole relaxation averaged over the entire bottle surface.

TABLE III. Bottleshift-fit coefficients.

Field	$\theta_m$	$\phi_m$	$\theta_Q$	$\phi_Q$	$E_Q$ ( $\mu\text{Hz}$ )	$E_0$ ( $\mu\text{Hz}$ )
-	60	109.48	80(2)	116(2)	129(6)	-85(4)
+	60	54.74	88(4)	112(4)	135(26)	-127(19)

On the other hand, the  $^{201}\text{Hg}$  could be strongly relaxed at surface imperfections due to electric field gradients and due to a higher-binding energy at these sites and hence a longer dwell time. The average over the rest of the surface contributes little to its observed relaxation rate. Thus, the apparent surface binding energy of the  $^{201}\text{Hg}$  seems greater than for the  $^{199}\text{Hg}$ .

We conclude that our technique allows us to understand the relaxation and energy-shift mechanisms associated with the bottle. The existence of a small quadrupole emerges clearly from rotating the cell, and its size can be measured accurately. The agreement among the various methods of estimating  $E_q$  is very good; note that the quadrupole calibration factor is a necessary part of this. Also, the angular variation of the temperature dependence of the energy shift is probably the most convincing evidence that the bottle shift is dominated by the quadrupole observed in the rotation measurements.

It is interesting to note that other workers have noticed an anomalous increase in the relaxation rates of Hg on fused silica in the range of 500–600 K, after which the relaxation rate decreases with temperature.<sup>15</sup> This has been attributed to a phase change in the fused silica. We have also observed this in cells constructed of low-purity commercial grade fused silica. However, in cells made of high-purity fused silica (Suprasil) we have always observed a monotonic decrease in relaxation rate with temperature (cf. the data in this section). The lifetimes reported in Ref. 15 are on the order of a few seconds; we obtained similar results with low-purity fused silica. In the case of low-purity cells the relaxation rate of the  $^{199}\text{Hg}$  is greater than that of the  $^{201}\text{Hg}$  (in the region of increasing relaxation rate). This indicates that magnetic interactions dominate the relaxation. Perhaps the differences in relaxation phenomena between high-purity and low-purity cells are due to the different (paramagnetic) sodium concentrations in fused silica.

## VI. EXPERIMENTAL TEST OF SPATIAL ISOTROPY AND INTERPRETATION OF RESULTS

### A. Motivation

According to the Einstein equivalence principle (EEP), a measurement (experimental result) made in a reference frame which is freely falling and is shielded from nongravitational interactions (e.g., electromagnetism or other known background fields) is not sensitive to gravitational fields generated by sources outside that reference frame (except for tidal effects which can be made negligible by making the measurement apparatus small enough).<sup>27,28</sup> We assume that self-gravitational effects of the measurement apparatus are negligible. Such frames are called local Lorentz frames and measurements made in such frames are called local nongravitational test experiments. The EEP is the foundation upon which all metric theories of gravity are based and requires universality, local position invariance, and local Lorentz invariance to hold for all local Lorentz frames. Universality requires that all forms of mass-energy couple to gravity in the same manner. For massive objects, this is the same as the

weak equivalence principle, as first stated by Newton, that all objects fall with the same acceleration in a gravitational field. Local position invariance requires that any experimental result be the same in any local Lorentz frame regardless of where and when in space time the experiment is performed. Local Lorentz invariance demands that any experimental results be invariant regardless of the orientation or velocity of the measurement apparatus relative to distant reference frames (e.g., the fixed stars).

We are interested in testing local Lorentz invariance (LLI) which requires that measurements made in a local Lorentz frame do not depend on the orientation of the apparatus in that frame. In particular we ask the question: Does the rest mass-energy of a nucleus depend on its orientation in space? One possibility that has been studied extensively is a dependence of the mass of a nucleus on the orientation of its nuclear-quadrupole moment  $Q$ .<sup>29–31</sup> If there is some special axis in space, the fraction of the nuclear mass-energy associated with  $Q$  (interaction of the valence nucleons and core polarization effects) could be a function of the orientation of  $Q$  relative to this special axis. There would then be an energy shift of the form

$$\delta(mc^2) = \delta_F E_S P_2(\cos\alpha), \quad (6.1)$$

where  $\delta_F$  is a dimensionless parameter which describes the magnitude of spatial anisotropy in the local frame,  $E_S$  is the energy associated with the orientable structure of the nucleus (i.e.,  $Q$ ),  $P_2(\cos\alpha)$  is the second-order Legendre polynomial, and  $\alpha$  is the angle between the nuclear-spin-quantization axis and the special axis in space. Note that the energy associated with the bare nuclear core does not contribute since the spherically symmetric core cannot be oriented.

Leitner and Lee<sup>32</sup> have developed a framework in which violations of LLI can be treated quite generally through an action principle. Called the  $TH\epsilon\mu$  model, it starts from the assumption that the EEP is a postulate which holds approximately and allows one to compute the observed size of a possible LLI-violating interaction which is generated by a small breaking of that postulate. In this model, material (massive) objects and photons propagate with different limiting velocities  $c_0$  and  $c$ , respectively. A measure of the breakdown of LLI is the parameter  $\eta = |1 - (c_0/c)^2|$ . While the laws of physics may take on a symmetric form in a special frame (e.g., the rest frame of the Universe), in a local frame moving relative to that special frame one observes a breakdown of LLI, with  $\delta_F$ , given by

$$\delta_F = (V/c)^2 \eta, \quad (6.2)$$

where  $V$  is the velocity of the local frame relative to the special frame. A useful feature of  $TH\epsilon\mu$  is that it allows comparison between very different experiments; the Michelson-Morley experiment, time-of-flight comparisons between photons and massive test particles, and experiments such as ours all measure the same property of space. There are, however, some limitations to  $TH\epsilon\mu$ . For example, only electromagnetic and gravitational in-

teractions are treated rigorously in this framework.

In our experiment, an energy anisotropy of the  $^{201}\text{Hg}$  nucleus of the form given by Eq. (6.1) would be manifest as a contribution to the quadrupole energy splitting  $\omega_Q$  introduced in Eq. (2.1). As in Eq. (2.2),  $\omega_Q$  will vary with orientation as  $P_2(\cos\alpha)$ , where  $\alpha$  is the angle between the applied magnetic field and the special axis in space. Since the magnetic field in our apparatus is fixed in the lab frame, which rotates relative to distant frames (because of the rotation of the earth),  $\omega_Q$  will have a modulation at twice the Earth's sidereal rotation frequency. (If instead there were a dipole coupling to a spatial anisotropy, it would produce frequency shifts that vary only at the sidereal frequency itself.)

Our apparatus shields the Hg nuclei from external electromagnetic fields. However, there may be other background fields to which we are sensitive. We are moving with respect to the rest frame of the big bang ( $V/c \approx 10^{-3}$ ) as indicated by the anisotropy of the 3-K microwave background. Thus any cosmic field remnant from the big bang will have a net flux relative to our apparatus. Such a field can produce observable effects in our apparatus if it couples to the spin or quadrupole moments of the Hg nuclei with sufficient strength. The same holds true for any as yet undiscovered field associated with emissions from stars, galaxies, or dark matter in the Universe. Such couplings are not removed by our magnetic field servo provided that they do not couple to  $^{199}\text{Hg}$  and  $^{201}\text{Hg}$  in exactly the ratio of their nuclear-magnetic moments. Thus our apparatus is also a sensitive antenna for detecting such new physics.

Using the notation developed in Sec. II, we consider spatial variations of the  $^{201}\text{Hg}$  nuclear Zeeman levels of the form

$$H = \nu_{10}\sqrt{5}T_{10}(\frac{3}{2})P_1[\cos(\alpha_1)] + \nu_{20}T_{20}(\frac{3}{2})P_2[\cos(\alpha_2)] , \quad (6.3)$$

where  $H$  is the Hamiltonian which describes the Zeeman splitting of the  $^{201}\text{Hg}$  nucleus,  $\alpha_1$  and  $\alpha_2$  are the angles between the quantization axis (which is always parallel to the Earth's equatorial plane) and possible dipole and quadrupole interactions at some preferred directions in space,  $\nu_{10}$  is the energy shift of the dipole interaction along its preferred direction, and  $\nu_{20}$  is the shift of the quadrupole interaction. Note that  $\nu_{10}$  is a combination of possible dipole shifts of the  $^{201}\text{Hg}$  and  $^{199}\text{Hg}$  Zeeman levels because the magnetic field stabilization forces the  $^{199}\text{Hg}$  Zeeman splitting to be constant. In general,  $\nu_{10} = \nu_{10}^{201} + (\gamma_{201}/\gamma_{199})\nu_{10}^{199}$ , where the Hamiltonian which described interactions with the  $^{199}\text{Hg}$  nucleus is

$$H = (\nu_1^{199}/\sqrt{2})T_{10}P_1[\cos(\alpha_1)] .$$

Thus, we are sensitive to dipole interactions only insofar as the ratio of the interaction strength between the two isotopes is different from the ratio of their  $g$  factors. The  $^{201}\text{Hg}$  nucleus is alone sensitive to quadrupole interactions.

We specify directions by the colatitude  $\Theta$  and longitude  $\Phi$  relative to the Earth's equatorial plane. Because

the quantization axis is always parallel to the equatorial plane ( $\Theta = \pi/2$ ) we can write the  $\Phi$ -dependent terms in Eq. (6.3) in the form

$$H = \nu_1\sqrt{5}T_{10}(\frac{3}{2})\cos(\Phi - \Phi_1) + \frac{4}{3}\nu_2T_{20}(\frac{3}{2})\cos 2(\Phi - \Phi_2) , \quad (6.4)$$

with

$$\nu_1 = \nu_{10}\sin\Theta, \quad \nu_2 = \nu_{20}\sin^2\Theta . \quad (6.5)$$

## B. Description of the experiment

The search for spatial anisotropy used the experimental apparatus described in Sec. III. The  $^{201}\text{Hg}$  and  $^{199}\text{Hg}$  were simultaneously operated as driven atomic-absorption oscillators as described previously. The bottle-related parameters were as described in Sec. V. The light-independent relaxation times were  $1/\gamma_1 = 1200 \pm 100$  sec for  $^{199}\text{Hg}$ , while for  $^{201}\text{Hg}$ ,  $2/\gamma_2 = 1/\gamma_1 = 80 \pm 5$  sec. Under the experimental conditions the light intensity dominated the relaxation, shortening these times to 80 and 50 sec, respectively, for  $^{199}\text{Hg}$  and  $^{201}\text{Hg}$ . Using the  $^{199}\text{Hg}$  phase to stabilize the magnetic field we looked for a variation in the  $^{201}\text{Hg}$  phase as the quantization axis of the apparatus rotated relative to the fixed stars, due to the rotation of the Earth. For this reason, the axis in Fig. 2 were oriented such that the  $y$  axis (the axis of the oscillating magnetic field) was parallel to the Earth's rotation axis. The  $z$  axis (pump-light axis) pointed east, and the  $x$  axis pointed inward toward the Earth's rotation axis. The quantization axis (the static magnetic field) thus lay in the plane perpendicular to the Earth's rotation axis. Anisotropy data were taken with two orientations of the quantization axis in the  $xz$  plane to test for diurnal systematic effects; letting  $\beta$  be the angle between the static magnetic field and the  $z$  axis in the  $xz$  plane, then the two orientations were  $\beta = 45^\circ$  and  $\beta = 135^\circ$  (plus and minus field configurations, respectively, for the discussion that follows). The field configuration shown in Fig. 2 corresponds to  $\beta = 45^\circ$ .  $\beta$  was changed by reversing the  $z$  component of the magnetic field while leaving the  $x$  component of the field unchanged.

Six data runs were taken, each of roughly 2.5-day duration. Three runs were taken in the plus field configuration and three for minus field. Before and after each run, calibrations of the dipole and quadrupole sensitivities of the apparatus were taken as described in Sec. IV. As described in Sec. III, the quadrature signal from the  $^{199}\text{Hg}$  PSD ( $V_{\text{out}}^{199}$ ) was used to stabilize the magnetic field to thus obtain a constant  $^{199}\text{Hg}$  precession frequency. Ideally,  $V_{\text{out}}^{201}$  would then be a measure of quadrupole couplings to the  $^{201}\text{Hg}$  and would be insensitive to fluctuations in the magnetic field. In reality, there are a number of mechanics that cause  $V_{\text{out}}^{201}$  to drift relative to  $V_{\text{out}}^{199}$ . In a typical run there was a  $100\text{-}\mu\text{Hz}$  drift in the  $^{201}\text{Hg}$  precession frequency.

The dominant source for the  $^{201}\text{Hg}$  frequency (or phase) drift were drifts in the lamp intensity of as much as 5% per 2.5-day run. The  $^{201}\text{Hg}$  phase drifts because

the light shifts due to the pump light are different for each isotope. If the ratio of the induced-light shifts for each isotope were equal to the ratio of their magnetic moments, then changes in light intensity would have the same effect on the respective resonance frequencies as a change in magnetic field. The correction circuit would then remove any frequency shifts associated with changes in light intensity. Because the  $^{204}\text{Hg}$  lamp frequency is further from the  $^{201}\text{Hg}$  absorption line center, the virtual light shift for  $^{201}\text{Hg}$  is about five times that of  $^{199}\text{Hg}$ , and the correction circuit does little to reduce light shifts. The output of the atomic oscillators can also change because the out-of-phase detector is insensitive to the in-phase signal only to some accuracy. When the light intensity changes, the in-phase signal amplitude changes, and these changes can either affect the correction signal or the  $^{201}\text{Hg}$  out-of-phase signal directly. Even at constant lamp intensity, drifts in the spatial and spectral distributions of lamp intensity can cause a shift of the  $^{201}\text{Hg}$  frequency.

Drifts in room temperature can affect amplifier phase and voltage offsets, the circular polarization of the light, and the temperature and heating currents in the oven. We used a 10-kHz ac current with feedback control to maintain oven temperature. Although the current path in the heating elements was coaxial, there was a small magnetic leakage field detectable in the oven. This leakage field will produce rf shifts of the resonance frequencies for the nuclear spins which do not scale in the same ratio as the magnetic moments and are hence not removed by the magnetic field servo. Oven temperature changes affect the  $^{201}\text{Hg}$  bottle shift by  $1 \mu\text{Hz}/^\circ\text{C}$  and can also affect the sensitivity and light shifts of the atomic oscillators.

During a run, we monitored the in-phase and out-of-phase signals from both atomic oscillators, the magnetic field correction signal, the lamp intensity, the room temperature, and the oven current. Each channel was sampled five times per second for 1 min, then averaged by a computer. After a run, we calculated an average and scatter for each consecutive 20-min interval. When calculating the scatter on the atomic oscillator channels we took into account the correlations due to electronic filter-

ing, atomic lifetimes, and computer averaging. Each 20-min interval is then treated as a statistically independent data sample in the data analysis.

### C. Data analysis

The dominant feature in the data was long-term drift caused by changes in the lamp intensity which varied by as much as 5% over the course of a run. The drift resulted in apparent real frequency shifts between the two isotopes on the order of  $100 \mu\text{Hz}$  total. Examples of apparent frequency shifts include changes in the atomic oscillator sensitivities coupled with the light shift and the bottleshift. An example of a real shift is the light shift itself which is proportional to the lamp intensity.

A simple model which accounts for the changing light intensity is based on the analysis of the spin- $\frac{1}{2}$  atomic oscillator presented in Appendix A. This analysis is approximately true for the spin- $\frac{3}{2}$  system. A change in the resonant frequency of the atomic oscillator relative to the (constant) drive frequency results in a phase shift between the light modulation and the magnetic driving field  $\delta\phi = \delta\omega/\Gamma$ , where  $\Gamma$  has contributions from both the pump light and wall relaxation. The phase shift results in a change in the out-of-phase voltage  $\delta V_{\text{out}} = V_{\text{in}} \delta\phi$ . We measured the sensitivity to dipole frequency shifts at the beginning of a run by changing the driven frequency by a small amount as previously discussed;  $\xi^{-1} = -\partial V_{\text{out}}/\partial\omega = -V_{\text{in}} \partial\phi/\partial\omega = -V_{\text{in}} \Gamma^{-1}$ . As the light intensity varies over the course of a run,  $\Gamma$ ,  $V_{\text{in}}$ , and  $\xi$  all vary. We found that including fit terms in our data analysis (to be discussed shortly) to describe changes in  $\Gamma$  did not significantly alter  $\chi^2$ ; changes in the sensitivity were due mainly to changes in  $V_{\text{in}}$ . Thus, if the initial sensitivity is  $\xi_0$ , at later times we take  $\xi(t) = \xi_0 V_{\text{in}}(0)/V_{\text{in}}(t)$ , which was verified experimentally. We verified experimentally and through numerical calculations that  $\eta$ , the relative quadrupole sensitivity, did not change significantly with small changes in light intensity.

In order to detect a possible anisotropy of the form of Eq. (6.4) and to account for various instrumental effects, we did a weighted fit to the function

$$\begin{aligned}
 f(t) \pm \sigma(f(t)) &= \xi_0 \frac{V_{\text{in}}^{201}(0)}{V_{\text{in}}^{201}(t)} [V_{\text{out}}^{201}(t) \pm \sigma(V_{\text{out}}^{201}(t))] \\
 &= a_0 + a_1 \cos(\Omega_{\oplus} t) + a_2 \sin(\Omega_{\oplus} t) + a_3 \cos(2\Omega_{\oplus} t) + a_4 \sin(2\Omega_{\oplus} t) \\
 &\quad + a_5 I(t) + a_6 \frac{V_{\text{in}}^{199}(0)}{V_{\text{in}}^{199}(t)} + a_7 \frac{V_{\text{in}}^{201}(0)}{V_{\text{in}}^{201}(t)} + a_8 \frac{V_{\text{out}}^{199}(t)}{V_{\text{in}}^{199}(t)} + a_9(t-t_0) + a_{10}(t-t_0)^2 + a_{11} T_{\text{room}}(t) + a_{12} i_{\text{oven}},
 \end{aligned} \tag{6.6}$$

where  $t$  and  $\sigma$  label the average of the time and the scatter for the 20 points.  $\xi_0$  is replaced by  $\xi_0/\eta$  to calibrate the data for quadrupole effects.  $a_1 - a_4$  are included to determine whether there is a spatial anisotropy.  $\Omega_{\oplus}$  is the sidereal rotation rate of the Earth, and  $t$  is the time in seconds. The direction of the quantization axis (which

lies in a plane perpendicular to the Earth's rotation axis) in space is  $\Phi = \Omega_{\oplus} t$ . We set  $\Phi = 0$  at 00:00:00 Pacific standard time, 12 March 1986.

The term  $a_5$  accounts for the light shift which is approximately proportional to the lamp intensity (neglecting changes in the spectral profile). This term is neces-

sary because the light shift for each of the isotopes is not in the ratio of the  $g$  factors.  $a_6$  accounts for a possible voltage offset in the stabilization-loop electronics. When the  $^{199}\text{Hg}$  atomic oscillator is exactly on resonance, the input to the integrator is zero to within a small offset  $\delta V$ . There must be a small phase shift in the atomic oscillator to give an out-of-phase voltage to cancel this offset;  $\delta V = \delta\phi' V_{\text{in}}(t) = \text{const}$ , giving rise to a frequency offset (magnetic field offset)  $\delta f = \delta\phi' \Gamma / 2\pi$ . Thus, as the  $^{199}\text{Hg}$  in-phase signal changes, there is a frequency shift  $\delta f = a_6 / V_{\text{in}}(t)$ . If there is a voltage offset in the out-of-phase signal of the  $^{201}\text{Hg}$  atomic oscillator, since we divide the in-phase by the out-of-phase signals to account for the change in sensitivity, there is a term  $a_7 / V_{\text{in}}(t)$ .  $a_8$  compensates for voltage-offset drifts in the field-stabilization-loop integrator.  $a_9$  and  $a_{10}$  are included to account for a quadratic baseline in the data; note that the inclusion of a quadratic baseline cannot interfere with a possible anisotropy signal, for it can cross zero at most twice, whereas the trigonometric functions cross zero at least three times over the duration of the experiment.  $a_{11}$  accounts for possible effects due to the room temperature changes which to first order should be linear.  $a_{12}$  accounts for a possible Bloch-Siegert shift between the isotopes due to a magnetic leakage field from the heater of about 0.1 mG at 10 kHz. This shift does not scale in the ratio of the  $g$  factors as a static field does.

We used multiple regression<sup>33</sup> to find the values of the coefficients which minimize  $\chi^2$ . The individual 20-min averaged data points were weighted by the scatter in  $V_{\text{out}}^{201}$  over that 20-min interval.

Figure 9 shows a plot of  $f$  and the results of the fit versus  $t$ . The (calibrated) raw data points (down-sloping curve) are shown with the fit residuals. These data are typical of the series of six runs. The assumed functional form is in excellent agreement with the data. For the series of data runs,  $\chi^2$  varied from 0.4 to 2, with the average very near 1. For the plot shown,  $\chi^2 = 1.0$ .

Some of the independent data channels had significant variations with Fourier amplitudes near  $\Omega_{\oplus}$  while none

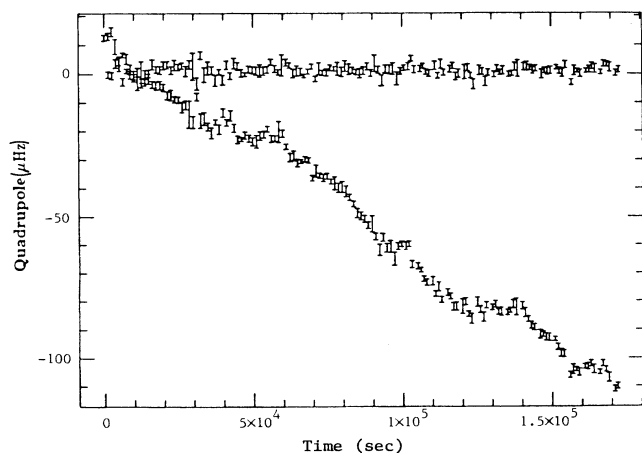


FIG. 9. Raw data for  $V_{\text{out}}^{201}$  (sloping curve) and after regression for a typical 2.5-day run.

had any discernable variations at  $2\Omega_{\oplus}$ . The  $\Omega_{\oplus}$  amplitude times the fit coefficient for a particular channel was always less than  $2 \mu\text{Hz}$ . The effects were always resolved to less than  $3\sigma$ . We will describe how we check whether the resolved variations generated or masked an anisotropy signal.

We did the fits three different ways: In method 1, all of the instrumental drifts were fit out of the data before the trigonometric functions were fit for each run separately. In method 2, all terms were fit at the same time. In method 3, we took the method-1 data (before fitting out the trig functions) and averaged it in “bins” corresponding to the direction of the quantization axis relative to possible fixed anisotropies in space. There are 72 bins of  $5^\circ$  each. The frequency for each angle of the quantization axis modulo  $360^\circ$  is placed in the appropriate bin; with the data from all six runs, there are 14 points per bin. For only the plus field or minus field data, there are about seven points per bin. The bins are averaged (weighted) and the scatter of the weighted average is multiplied by  $\chi^2$  for the average (if  $\chi^2$  is greater than 1). Method 3 takes fullest advantage of the temporal coherence of any possible anisotropy signal over the separate runs.

The results of method 1 are given in Table IV along with the results of fitting the trigonometric functions to the raw (calibrated) data (no drifts taken out). In these analyses, any time  $\chi^2$  for a particular operation is greater than 1, the uncertainty according to that operation is multiplied by  $(\chi^2)^{1/2}$  to account for uncertainties in the “goodness” of the fit.

The results of method 2 are given in Table V. Note that the  $1\Omega_{\oplus}$  fit coefficients have larger error bars than those of method 1, while the  $2\Omega_{\oplus}$  coefficients are in fairly good agreement. This is probably due to the presence of  $1\Omega_{\oplus}$  variations in some of the data channels.

The results of method 3 are shown in Figs. 10–12. The trigonometric functions were fit to each set of binned or “wrap-around” data; both the quadrupole and dipole wrap arounds were fit to all four trigonometric functions. The values of  $a_1$  and  $a_2$  are the fit coefficients from the dipole wrap around while  $a_3$  and  $a_4$  are the fit coefficients from the quadrupole wrap around. These results are also listed in Table IV (e)–(g). Note the good agreement to the average of the trigonometric coefficients of the method-1 analysis.

As mentioned previously, several of the independent data channels had large  $\approx 1\Omega_{\oplus}$  variation. In the linear regression, this variation can project onto the  $1\Omega_{\oplus}$  functions. In order to test whether a possible anisotropy would be “masked” by these variations, we added a “false anisotropy effect” to the data and repeated the fit. Basically, we added either  $\delta f \sin(\Omega_{\oplus} t)$ ,  $\delta f \cos(\Omega_{\oplus} t)$ , or their  $2\Omega_{\oplus}$  counterparts, (each separately) to the calibrated data and did the fits exactly as before. We found that both methods 1 and 2 gave  $\delta f$  for the  $2\Omega_{\oplus}$  coefficients to well within the fit uncertainties (about 20%), while  $\delta f$  for the  $1\Omega_{\oplus}$  coefficients were too small by a factor of 0.5 for the method-1 results and a factor of 2 too large for the method-2 results. Because of this, the result we will quote for the  $1\Omega_{\oplus}$  amplitude will be based on the average of methods-3 and -2 coefficients (for all data; the field

TABLE IV. Method-1 analysis results.  $a(1)$  and  $a(2)$  are calibrated in dipole  $\mu\text{Hz}$ , while  $a(3)$  and  $a(4)$  are calibrated in quadrupole  $\mu\text{Hz}$ . Values in parentheses denote uncertainties.

Run	$a(1)$	$a(2)$	$a(3)$	$a(4)$
(a) Raw data				
13p	9.14(2.29)	27.11(2.36)	6.44(2.07)	-0.65(2.00)
16m	8.06(4.34)	-8.56(4.42)	13.13(4.35)	1.35(3.99)
19p	-3.05(2.72)	1.58(2.58)	8.07(5.32)	7.95(4.84)
23p	0.20(1.01)	2.40(0.96)	0.68(1.96)	1.89(1.89)
25m	-7.25(0.86)	-1.13(0.85)	5.32(1.58)	2.93(1.59)
29m	-6.07(1.12)	-12.09(1.25)	0.07(1.80)	-5.91(1.72)
Av	-3.60(2.32)	-0.58(4.12)	3.73(1.68)	-0.04(1.87)
$\chi^2$	18.78	59.27	3.65	4.79
(b) Drifts out, all data				
13p	-0.21(0.28)	-0.03(0.28)	0.16(0.27)	0.00(0.26)
16m	0.05(0.19)	-0.26(0.20)	0.19(0.20)	0.41(0.18)
19p	-0.38(0.26)	-0.03(0.25)	-0.08(0.31)	-0.27(0.28)
23p	-0.08(0.16)	0.00(0.15)	0.15(0.31)	-0.56(0.30)
25m	0.01(0.10)	-0.02(0.10)	-0.14(0.19)	0.52(0.19)
29m	0.00(0.25)	0.00(0.28)	-0.29(0.37)	0.65(0.36)
Av	-0.05(0.07)	-0.05(0.07)	0.02(0.10)	0.21(0.19)
$\chi^2$	0.64	0.34	0.68	3.92
(c) Drifts out, field plus				
13p	-0.21(0.28)	-0.03(0.28)	0.16(0.27)	0.00(0.26)
19p	-0.38(0.26)	-0.03(0.25)	-0.08(0.31)	-0.27(0.28)
23p	-0.08(0.16)	0.00(0.15)	0.15(0.31)	-0.56(0.30)
Av	-0.17(0.12)	-0.01(0.12)	0.08(0.17)	-0.24(0.23)
$\chi^2$	1.03	0.02	0.43	2.06
(d) Drifts out, field minus				
16m	0.05(0.19)	-0.26(0.20)	0.19(0.20)	0.41(0.18)
25m	0.01(0.10)	-0.02(0.10)	-0.14(0.19)	0.52(0.19)
29m	0.00(0.25)	0.00(0.28)	-0.29(0.37)	0.65(0.36)
Av	0.01(0.09)	-0.07(0.09)	-0.01(0.18)	0.48(0.12)
$\chi^2$	0.03	1.18	2.06	0.46
(e) Wrap around, all data				
All	-0.04(0.08)	-0.11(0.08)	-0.05(0.10)	0.13(0.10)
$\chi^2$	1.10			
(f) Wrap around, field plus				
Plus	-0.13(0.14)	-0.11(0.14)	-0.20(0.20)	-0.34(0.20)
$\chi^2$	1.87			
(g) Wrap around, field minus				
Minus	-0.06(0.11)	-0.14(0.11)	-0.02(0.15)	0.44(0.14)
$\chi^2$	0.37			

plus, minus results will be used to estimate systematics) with the uncertainty in final coefficients the average of the fit uncertainties. For the  $2\Omega_{\oplus}$  amplitude, we take the coefficients from the method-3 analysis since these are in agreement with all other methods of analysis, treat the data most equally, and take greatest advantage of the temporal coherence of any true anisotropy signal across all runs. Thus, the results (in terms of the total amplitudes), before correction for systematic errors are [see Eqs. (6.4) and (6.5)]

$$v_1 = 0.53 \pm 0.38 \mu\text{Hz}, \quad v_2 = 0.17 \pm 0.13 \mu\text{Hz},$$

where the amplitude is given by the square root of the sum of the squares of the sin and cos fit coefficients.

#### D. Systematic effects

The anisotropy signal we look for could be mimicked or masked by fluctuations in the experimental apparatus which occur at harmonics of 1 per *solar day*. Because the solar and sidereal day are different, one could isolate the anisotropy signal from diurnal fluctuations by separating the measurements over the course of a year. However, this works only if the fluctuations show no seasonal

TABLE V. Method 2 analysis results.  $a(1)$  and  $a(2)$  are calibrated in dipole  $\mu\text{Hz}$  while  $a(3)$  and  $a(4)$  are calibrated in quadrupole  $\mu\text{Hz}$ .

Run	$a(1)$	$a(2)$	$a(3)$	$a(4)$
(a) All data				
13p	-1.65(1.09)	1.46(1.88)	-0.14(0.43)	0.14(0.36)
16m	1.37(1.33)	-0.71(0.66)	0.30(0.30)	0.67(0.26)
19p	-2.31(0.62)	0.79(0.62)	-0.52(0.37)	-0.32(0.31)
23p	-1.32(1.12)	1.23(1.20)	-0.40(0.53)	-0.99(0.43)
25m	0.06(0.80)	-0.59(0.73)	-0.12(0.45)	0.72(0.22)
29m	1.30(1.50)	0.97(1.12)	-0.47(0.47)	1.10(0.48)
Av	-1.03(0.67)	0.16(0.41)	-0.15(0.16)	0.35(0.29)
$\chi^2$	3.04	1.41	0.99	5.38
(b) Field plus				
13p	-1.65(1.09)	1.46(1.88)	-0.14(0.43)	0.14(0.36)
19p	-2.31(0.62)	0.79(0.62)	-0.52(0.37)	-0.32(0.31)
23p	-1.32(1.12)	1.23(1.20)	-0.40(0.53)	-0.99(0.43)
Av	-1.99(0.49)	0.93(0.53)	-0.37(0.25)	-0.32(0.42)
$\chi^2$	0.70	0.19	0.45	4.06
(c) Field minus				
16m	1.37(1.33)	-0.71(0.66)	0.30(0.30)	0.67(0.26)
25m	0.06(0.80)	-0.59(0.73)	-0.12(0.45)	0.72(0.22)
29m	1.30(1.50)	0.97(1.12)	-0.47(0.47)	1.10(0.48)
Av	0.56(0.63)	-0.40(0.60)	0.03(0.32)	0.74(0.16)
$\chi^2$	1.00	1.79	2.05	0.64

dependence. We chose instead to rotate the quantization axis by  $90^\circ$  between various runs. The difference in phases between the anisotropy and background signals allowed us both to isolate any anisotropy effect and to determine the size of any systematic contributions from the apparatus. These systematic effects are normally reduced by combining the results of different runs with proper phasing for the anisotropy signals. This flip changes the phase of a  $1\Omega$  anisotropy by  $90^\circ$  and a  $2\Omega$  anisotropy by  $180^\circ$ . This flip also changes the sign and magnitude of the cell quadrupole frequency shift. It also affects the light shift; the dipole light shift changes sign while the quadrupole light shift is unaffected. Most importantly, the quadrupole sensitivity changes sign while the dipole sensitivity stays the same. The net results of a field flip on the sign of the various effects are

$$2\Omega = +1 ,$$

$$\text{light dipole} = -1 ,$$

$$\text{light quadrupole} = -1 ,$$

bottleshift/temp dependence

$$= +1 \times (\text{magnitude change}) ,$$

and a  $90^\circ$  phase change on a dipole spatial anisotropy. This is assuming that any systematic varies in the same way on any given day.

Combining the results of the fits gives the possible systematic amplitudes

$$a_1^{\text{sys}} = \frac{a_1^+ - a_2^-}{2} = -0.8 \pm 0.4 \mu\text{Hz} ,$$

$$a_2^{\text{sys}} = \frac{a_1^- + a_2^+}{2} = 0.8 \pm 0.4 \mu\text{Hz} ,$$

$$a_3^{\text{sys}} = \frac{a_3^+ - a_3^-}{2} = -0.2 \pm 0.2 \mu\text{Hz} ,$$

$$a_4^{\text{sys}} = \frac{a_4^+ - a_4^-}{2} = 0.4 \pm 0.2 \mu\text{Hz} .$$

There are essentially no systematics to within the  $2\sigma$  confidence level. However, if we assume that these values do represent possible systematics due to the light-dipole, light-quadrupole and the cell-quadrupole shifts, we can make comparisons to what is known experimentally.

Since the temperature dependence of the quadrupole shift associated with the cell is about  $1 \mu\text{Hz}/^\circ\text{C}$ , an oven temperature variation with a  $1\Omega$  periodicity could give a systematic at that frequency. Since the magnitude of that variation would be different for the two field configurations for the same temperature variations one could not, in general, expect an exact cancellation for the two configurations. However, we estimate that the maximum temperature drift in our oven is less than  $0.2^\circ\text{C}$ , and the  $1\Omega_\oplus$  and  $2\Omega_\oplus$  components of this change are small compared to our statistical uncertainties.

The dipole and quadrupole effects of the light shift both add in one field configuration and subtract in the other, so the possible systematics from the light would cancel for the two field configurations to some degree of accuracy. To set limits on this systematic, we varied the pump-light intensity between runs. It is difficult to measure with our apparatus exactly how much light was ac-

tually affecting the atoms for a given setting of the aperture (focusing effects, etc.) so the relative light intensity for each run is not known to any precision; however, there is no large systematic associated with any run. The light intensities for the runs 23*p* and 29*m* were about 2.5 times greater than the rest of runs (the rest were at about an equal intensity). These two runs show no greater systematic than any other.

We conclude that the uncertainty of the  $1\Omega$  amplitude includes contributions from systematics. By taking the ratios of the anisotropy-sensitive and systematic-sensitive fit amplitudes, we conclude that the systematics on the  $2\Omega$  amplitude have probably been reduced by about a factor of 5 by the field flip, leaving  $0.04 \mu\text{Hz}$ . Also, from the raw fit coefficients, there a possible maximum systematic from the light of about  $1 \mu\text{Hz}$  which gets reduced by about a factor of 6 by the regression, and by another factor of  $\sqrt{6}$  because we have 6 runs (the  $2\Omega$  light noise is not coherent between the runs), leaving a maximum total light systematic of about  $0.09 \mu\text{Hz}$ . Thus the final ampli-

tudes we quote are

$$\nu_1 = 0.53 \pm 0.38 \mu\text{Hz}, \quad \nu_2 = 0.17 \pm 0.17 \mu\text{Hz}, \quad (6.7)$$

where the uncertainty reflects both statistics and systematics.

We had originally planned to flip the field about every 20 min to cancel possible systematics; from this discussion we can see that some of the possible systematics change in the same way as a spatial anisotropy. For example, if the light intensity changed, the sensitivity and light shifts both change. Although a field flip would cancel these two effects, the change in sensitivity coupled with the change in cell quadrupole shift would add a frequency change. As the lamp drifts over a day, the frequency difference signal would still show drifts associated with the light. Thus, it would be necessary to flip the field and simultaneously hold all angles between the magnetic fields, the relevant light-shift axes, and the cell orientation constant. This was not possible in our apparatus. Furthermore, flipping the field would have in-

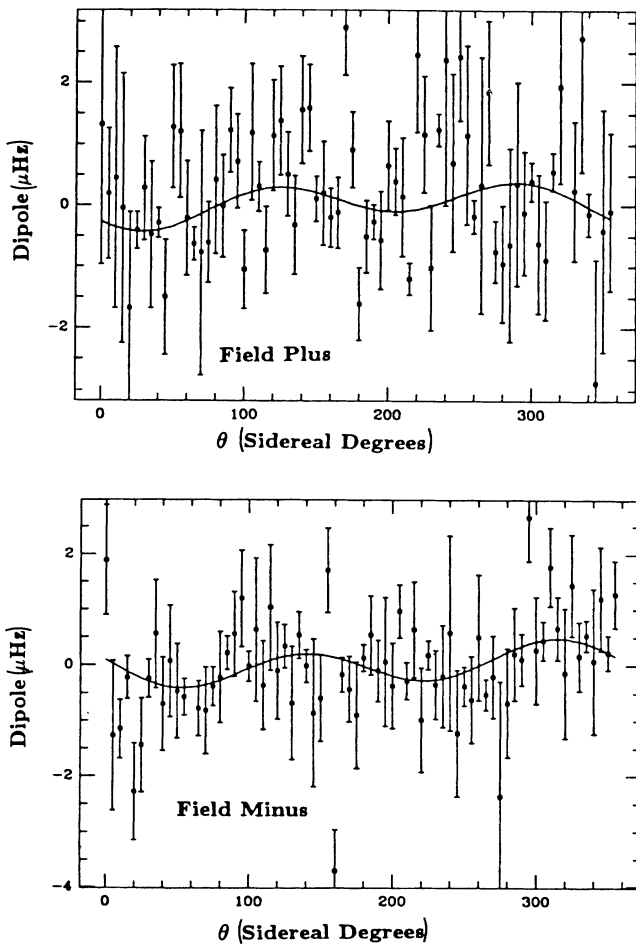


FIG. 10 Binned data, dipole sensitive. Entire set of field plus and field minus data is averaged into  $5^\circ$  bins modulo one sidereal day. The solid curves are the fits to Fourier components at  $\Omega_\oplus$  and  $2\Omega_\oplus$ .

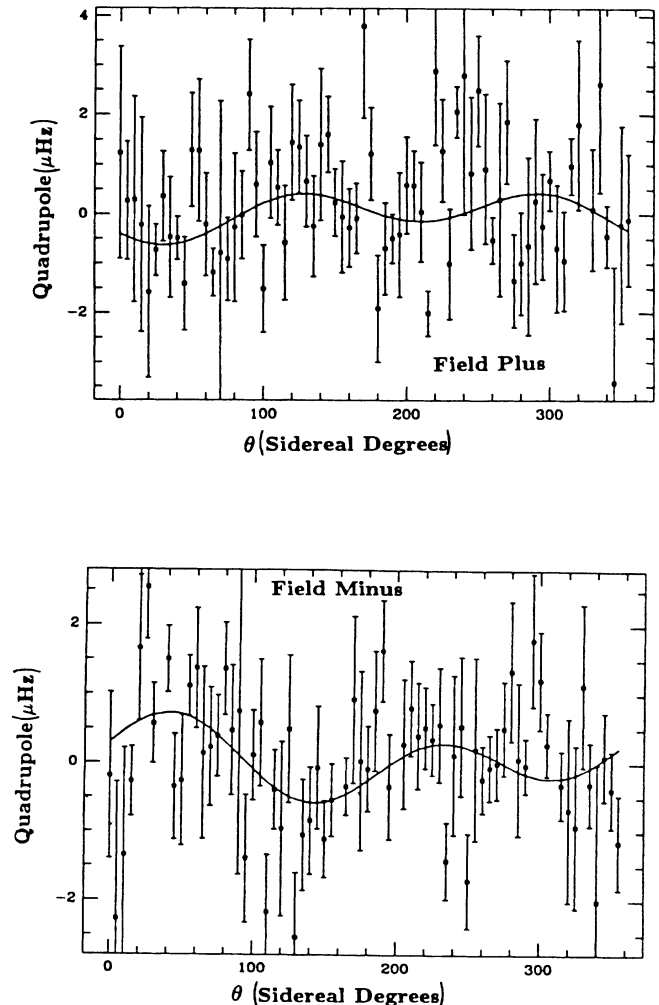


FIG. 11. Binned data, quadrupole sensitive.

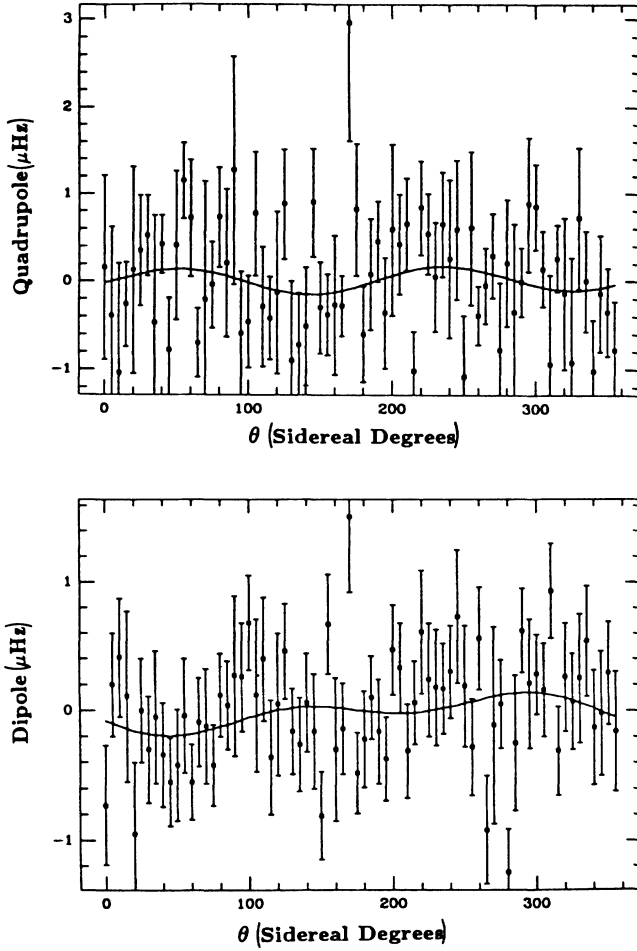


FIG. 12. Combined binned data.

produced a large “dead time” in the experiment to allow the atomic oscillators and magnetic field servo to relax to a new steady state after each flip.

### E. Experimental results and significance

Referring to Eqs. (6.4), (6.5), and (6.7), we can express our final result as follows:

$$E_{10} = h\nu_{10} = [(2.2 \pm 1.6) \times 10^{-21} \text{ eV}] / \sin\Theta_1,$$

$$E_{20} = h\nu_{20} = [(0.7 \pm 0.7) \times 10^{-21} \text{ eV}] / \sin^2\Theta_2.$$

Since we do not resolve any effect, we leave  $\Phi_1$  and  $\Phi_2$  unspecified.

Using the  $TH\epsilon\mu$  formalism and Eqs. (6.1) and (6.2), we can write  $E_{20}$  in terms of the LLI-breaking parameter  $\eta$ ,<sup>31</sup>

$$E_{20} = \eta \frac{(Z-1)e^2Q}{6R^3} (V/c)^2,$$

where  $Z$ ,  $Q$ , and  $R$  are, respectively, the proton number, quadrupole moment, and charge radius of the  $^{201}\text{Hg}$  nucleus,  $e$  is the electronic charge, and  $V/c \approx 10^{-3}$  is the velocity of the Earth relative to the frame in which the 3-K microwave background is isotropic. Our result yields  $\eta \leq 5 \times 10^{-22}$  and implies  $|c - c_0| \leq 3 \times 10^{-22}c$ .

These results represent a 2000-fold increase in sensitivity over the recent experiment of Prestage *et al.*<sup>31</sup> and a  $4 \times 10^5$  increase over Highes *et al.*<sup>29</sup> and Drever.<sup>30</sup> Recent limits from Michelson-Morley-type experiments<sup>34</sup> give  $\eta \leq 3 \times 10^{-9}$ . (Michelson-Morley experiments test LLI in a different way from ours, by measuring an anisotropy in the velocity of light. They can be compared to ours only in terms of a specific theory, such as  $TH\epsilon\mu$ .)

$E_{10}$  is a measure of any spatial anisotropy which arises from vector quantities used to describe the local frame. Such anisotropy can arise from some new background field as mentioned previously, or from anomalous couplings to gravity. It has been suggested that if Einstein equivalence were broken in the coupling of gravity to the intrinsic spins of elementary particles then there may exist interactions of the form<sup>35–37</sup>

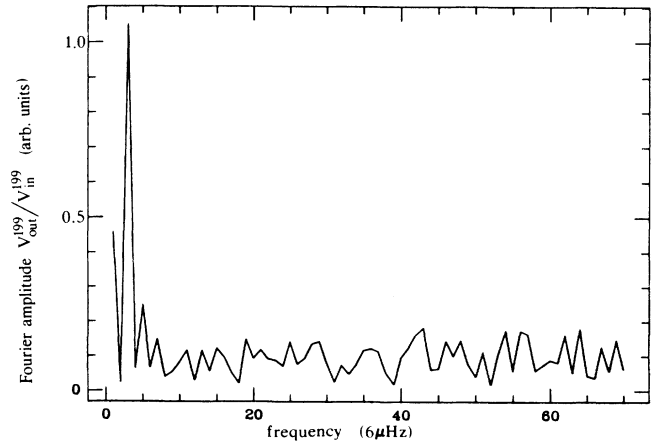
$$U_1 = \alpha_1 (g\hbar/2c) \boldsymbol{\sigma} \cdot \mathbf{R} / R,$$

$$U_2 = \alpha_2 (g\hbar/2c) \boldsymbol{\sigma} \cdot \mathbf{V} / c,$$

where  $g$  is the gravitational acceleration of the local frame due to a source labeled by position and velocity  $\mathbf{R}$  and  $\mathbf{V}$ , respectively, and  $\alpha_1$  and  $\alpha_2$  are dimensionless interaction strengths.  $U_1$  and  $U_2$  describe, respectively,  $T$ -odd- $P$ -odd and  $T$ -even- $P$ -odd gravitational couplings to intrinsic spin. If, for example, we use the sun as our source mass ( $g\hbar/2c = 2.6 \times 10^{-26}$  eV), we obtain  $\alpha_1 \leq 1 \times 10^5$  and  $\alpha_2 \leq 1 \times 10^9$ . Although the  $\alpha$ 's are expected to be of order 1 for maximal breaking of these discrete symmetries, these are nonetheless the best current limits for such couplings to intrinsic spin.

### F. Noise

We can determine the major noise sources in the apparatus by considering the noise on the various data channels and the noise frequency spectra in Figs. 13 and 14.

FIG. 13. Fourier transform of the  $V_{\text{out}}^{199}/V_{\text{in}}^{199}$  signal for a typical 2.5-day run.

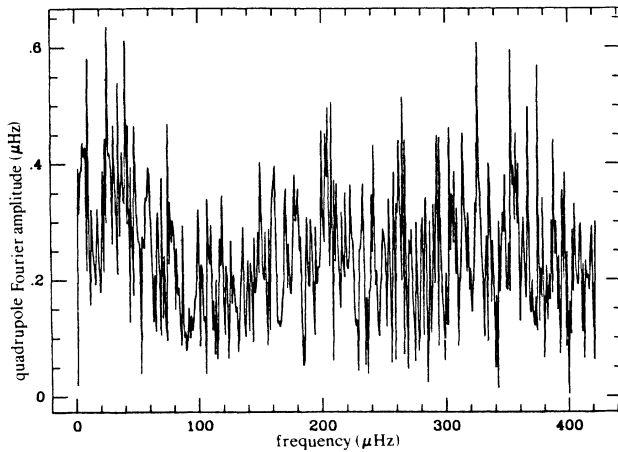


FIG. 14. Fourier transform of the entire set of data.

Figure 13 is a plot of the fast-Fourier transform (FFT) of the  $V_{\text{out}}^{199}/V_{\text{in}}^{199}$  data. Figure 14 is a plot of the binned wrap-around data (method 3) calibrated in quadrupole  $\mu\text{Hz}$ . Before the correlations with auxiliary data channels are removed in the regression analysis the FFT shows increasing noise at low frequencies. After the regression this excess low-frequency scatter is removed leaving a mostly white-noise spectrum with an rms amplitude consistent with the scatter estimated for the individual 20-min-averaged data points. The interesting exception to this white spectrum is the fairly broad peak in Fig. 14 which occurs with a period of about 1 h. We attribute this peak to disturbances associated with extra traffic in the building during hourly class changes. This peak has little effect on the statistical uncertainties of the anisotropy Fourier components.

We can compare the ratio of the measured noise power on the two atomic absorption oscillators to what we would expect for various models of the limiting noise source. In particular consider (1) a random-noise source which affects both oscillators in the same manner, (2) frequency jitter due to noise on the light shift, and (3) magnetic field noise. We expect the following noise power ratios for these noise sources:

$$\begin{aligned} \left[ \frac{(\delta V_{\text{out}}^{201})^2}{(\delta V_{\text{out}}^{199})^2} \right]_1 &= 1, \\ \left[ \frac{(\delta V_{\text{out}}^{201})^2}{(\delta V_{\text{out}}^{199})^2} \right]_2 &= 25, \\ \left[ \frac{(\delta V_{\text{out}}^{201})^2}{(\delta V_{\text{out}}^{199})^2} \right]_3 &= 0.05. \end{aligned}$$

Noise source (1) can arise from fluctuations in lamp power (not counting the effect on the light shift), or noise in the detection electrons. Noise source (2) arises from frequency shifts generated by lamp fluctuations. This is larger on the  $^{201}\text{Hg}$  oscillator because of its large light shift. Noise source (3) also produces frequency shifts but is smaller for  $^{201}\text{Hg}$  because of its smaller magnetic mo-

ment. In all cases one must take proper account of the magnetic servo action to derive the proper ratio of noise powers.

From our data we measure that the ratio of noise powers is 25. Thus we conclude that the limiting noise source was jitter in the light shifts induced by lamp fluctuations. This conclusion is consistent with estimates derived from other data channels. It is interesting that the short-term light-shift noise was not appreciably reduced by the regression analysis which included the lamp intensity. This could occur because the light intensity fluctuations underwent different phase shifts from the atomic oscillators. Second, changes in the lamp characteristics not reflected accurately by light intensity alone could account for this. For example, changes in the lamp temperature cause changes in the  $^{204}\text{Hg}$  density, which alters the spectral characteristics of the lamp (self-reversal), which leads to relative light shifts that do not scale with the lamp intensity. Also, changes in lamp power change other parameters of the oscillators (such as relaxation rates). The dominant fluctuations removed by the regression are long-term drifts which could be accounted for by a different value of the coefficient  $a_3$  than that needed to account for shorter-term fluctuations.

### G. Improvements

The limiting source of noise in the present experiment is due to fluctuations in the light intensity and spectral profile coupling through the light shift. These fluctuations seem to be Gaussian. A more sophisticated data analysis would probably not improve our current results as  $\chi^2$  is very near 1 with our simple linear model. Stabilization of the light source would probably be more helpful. However, it was difficult to achieve the stability we had with a microwave-discharge resonance lamp. One could use a stabilized laser source since only low-output power is required. Furthermore it could be possible to tune the laser to obtain a better ratio of light shifts for the two atomic-absorption oscillators.

The use of enriched isotopes in a larger absorption cell with a buffer gas would be helpful. Enriched isotopes would increase the signal amplitude by a factor of 5. A larger absorption cell would give a longer lifetime (scales as  $r$ , the cell radius); a lower pump rate can be used. Since the number of atoms required for one absorption length of the resonance light across the cell increase as  $r^2$ , so also must the number of photons per lifetime. Thus, since the cell cross-sectional area increases as  $r^2$ , the light intensity decreases as  $1/r$ , giving a lower light shift. A larger cell would also have a lower bottleshift (scales as cell area per cell volume). A cell containing a buffer gas would probably have both a lower bottleshift (increased diffusion time) and possibly a reduced light shift. Collisional broadening of the resonance line would decrease the light shift; however, the broadened line would absorb the photons less effectively increasing the Hg density necessary for one absorption length, thus increasing the necessary light intensity. Since the width increases linearly with the buffer-gas pressure while the absorption cross section decreases quadratically with the pressure,

there is a buffer pressure that will lead to a net minimum light shift (the increasing linewidth lowers the virtual light shift while the necessary increase in intensity raises the light shift).

There are several other possibly ways to reduce the light shift. One is to modulate the circular polarization (CP) of the pump light at the Larmor frequency and operate the system as a synchronously pumped atomic oscillator. The dipole light shift is zero to the extent that the CP averages to zero and the quadrupole light shift can be zeroed by proper choices of magnetic field direction and polarizer orientation (the quadrupole light shift depends on how the CP is modulated). This change would be relatively straightforward in the present apparatus. Another possibility is to use a free-precession technique in a pump-probe sequence as described in Sec. IV. By using separate pump and detection lamps and using an RF pulse to rotate the polarized atoms after the pump sequence, it would not be necessary to switch the static fields within the magnetic shield.

Another improvement would be to design an apparatus where changes in the quantization axis orientation are accomplished by a rotation of the entire apparatus in the lab. Changing the orientation at a rate different from and much faster than  $\Omega_{\oplus}$  would reduce the effects of both diurnal fluctuations and long-term drifts in the apparatus. We had originally planned to flip the magnetic field direction rapidly in the current experiment; the discussion in Sec. VI D shows that this probably would have not worked very well. However, a rotation of the entire apparatus would keep the relative angles of the light, cell, and magnetic field constant. This rotation would also allow a search for a possible anisotropy in any direction in space, whereas with the current apparatus we are sensitive only to the projection perpendicular to the Earth's rotation axis.

The main perturbations arising from rotating the apparatus would be magnetic perturbations and a gyroscopic effect due to the Earth's rotation. The gyroscopic effect is due to the additional apparent precession of the spins by the rotation of the Earth; both species have the same change in frequency. Thus the shift is not in the ratio of the  $g$  factors, and the magnetic field correction will not reduce it. If the magnetic field is stabilized by the  $^{199}\text{Hg}$  atoms, the  $^{201}\text{Hg}$  atoms will have an apparent frequency shift  $\delta\omega_{201} = (1 - \gamma_{201}/\gamma_{199})\Omega_{\oplus}\cos\theta$ , where  $\theta$  is the angle between the magnetic field and the Earth's rotation axis. Both the magnetic perturbations and  $\delta\omega$  would be modulated at the rotation frequency, while possible spatial anisotropies would be modulated at one and two times the rotation frequency (assuming the rotation rate is much faster than one per day) with the modulation amplitude varying at the rates  $\Omega_{\oplus}$  and  $2\Omega_{\oplus}$  (since the rotation plane of the apparatus is fixed on the rotating Earth). The magnetic field stabilization would probably remove effects due to external magnetic perturbations; in order not to add noise to the anisotropy signal, the gyroscopic signal will have to be stable over times on the order of a day.

The shot-noise estimate of the ultimate sensitivity can be made as follows: We have about  $10^{12}$  polarized atoms;

the lifetimes are on the order of  $\tau=100$  sec, so we can have a photon flux of  $10^{10}$ /sec to interrogate the atoms, giving a signal to noise of  $S/N=10^5 \text{ sec}^{1/2}$ . The linewidth can be split to  $(1/\pi\tau)(S/N)^{-1}$ , so in one hour,  $\delta\nu \approx 1$  nHz. If we take 24 points over a day and fit to the possible spatial anisotropies, we would get about 0.2 nHz for a day. This is over a factor of 1000 improvement on the present experimental result.

The shot noise for the present experiment can also be estimated. The light-collection and -detection efficiency is about 2% ( $=\epsilon$ ) (20% for the light pipe, 10% for the photomultiplier). The 2% ( $=\Delta I/I$ ) modulation of the light is on  $10^{10}$  photons/sec (there are  $10^{12}$  atoms in the cell, each of which scatters one photon in about 100 sec). Assume that all light that does not contribute to the signal is "useless" (does not relax or pump) and has a flux of  $10^{10}I/\Delta I$  photons/sec. Thus, we can estimate a signal to shot-noise ratio of  $S/N = (10^{10}\epsilon\Delta I/I)^{1/2} = 2000$ . Using a lifetime of 50 sec, we find that, in one day,  $\delta\nu = 10$  nHz. We are about a factor of 50 larger than this for the  $2\Omega$  limit.

#### APPENDIX A: SOLUTION FOR THE SPIN- $\frac{1}{2}$ ATOMIC OSCILLATOR

Because a spin- $\frac{1}{2}$  system has only scalar and dipole multipole moments, a complete description of the system can be given in terms of an ensemble of classical magnetic dipole moments which precess in a given magnetic field. Terms can be included to describe optical pumping and the decay of polarization.

The absorption of light by the ensemble of spin- $\frac{1}{2}$  atoms can be written in the form

$$\Delta I = \sigma \hat{k} \cdot \mathbf{P} ,$$

where  $\sigma = \pm 1$  for left or right circularly polarized light (we assume in this discussion that the light is perfectly circularly polarized),  $\hat{k}$  is the propagation direction vector of the light,  $\mathbf{P} = \mathbf{D} = 2\langle \mathbf{s} \rangle$  represents the atomic dipole polarization, and  $\Delta I$  is the light absorbed by the atoms.

To discuss the oscillator, the coordinate system in Fig. 15 will be used. The optical pumping can be modeled as follows:

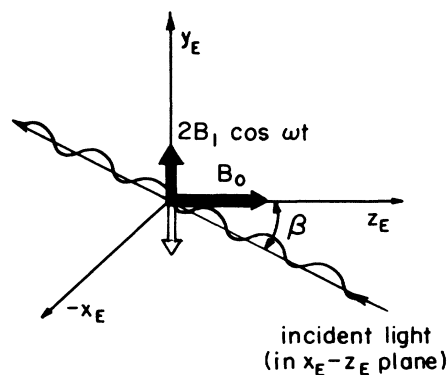


FIG. 15. Coordinate system used to describe the atomic oscillator.

$$\left( \frac{d\mathbf{P}}{dt} \right)_{\text{light}} = \Gamma_p (\sigma \hat{\mathbf{k}} - \mathbf{P}),$$

where  $\Gamma_p$  is the pump rate of the light. The decay of polarization can be described by

$$\left( \frac{d\mathbf{P}}{dt} \right)_{\text{relax}} = -\frac{1}{T_2} \mathbf{P},$$

where  $T_1$ , the longitudinal relaxation, time is assumed to equal  $T_2$ , the transverse relaxation time, as applies to the case of a small uniform magnetic field.

Finally, the total system evolution in the presence of a magnetic field is given by

$$\frac{d\mathbf{P}}{dt} = \Gamma_p (\sigma \hat{\mathbf{k}} - \mathbf{P}) - \frac{1}{T_2} \mathbf{P} + \gamma \mathbf{P} \times \mathbf{B}(t),$$

where  $\gamma$  is the gyromagnetic ratio, and  $\mathbf{B}(t) = B_0 \hat{\mathbf{z}}_E + 2B_1 \cos(\omega t) \hat{\mathbf{y}}_E$ .

The steady-state solution to this equation is most readily found by transforming to a coordinate system rotating at a rate  $\omega$  about  $\hat{\mathbf{z}}_E$  ( $\omega = \omega \hat{\mathbf{z}}_E$ ). The oscillating magnetic field can be written as the sum of two counter-rotating fields. The component that rotates opposite the spins (in the rotating frame) time averages to zero and can be neglected (the secular approximation).

To transform vectors to the rotating frame we need the matrix which describes rotations about  $\hat{\mathbf{z}}_E$

$$R = \begin{pmatrix} \cos(\omega t) & \sin(\omega t) & 0 \\ -\sin(\omega t) & \cos(\omega t) & 0 \\ 0 & 0 & 1 \end{pmatrix},$$

with  $R^{-1}$  given by the above with  $\omega$  replaced by  $-\omega$ .

The time derivative of a vector in the rotating frame is given by

$$\left( \frac{d\mathbf{P}}{dt} \right)_{\text{space}} = \left( \frac{d\mathbf{P}}{dt} \right)_{\text{rot}} + \omega \times \mathbf{P}.$$

Transforming  $\hat{\mathbf{k}} = (\sin(-\beta), 0, \cos\beta)$  and  $\mathbf{B}$  to the rotating frame and neglecting the oscillating terms, we find that near resonance  $\mathbf{P}$  in the rotating frame is described by

$$\frac{d\mathbf{P}}{dt} = \Gamma_p (\sigma \cos\beta \hat{\mathbf{z}}_E - \mathbf{P}) - \frac{1}{T_2} \mathbf{P} + \mathbf{P} \times (\Delta\omega \hat{\mathbf{z}}_E + \omega_1 \hat{\mathbf{y}}_E), \quad (\text{A1})$$

where  $\omega_1 = \gamma B_1$ ,  $\Delta\omega = \gamma B_0 - \omega$ , and  $\Delta\omega \leq \omega_1 \approx \Gamma_p \approx 1/T_2 \ll \omega$ .

Equation (A1) can be readily solved in the steady state,

$$0 = \Gamma_p \sigma \cos\beta - \Gamma_p P_{z_E} - P_{z_E}/T_2 - P_{x_E} \omega_1,$$

$$0 = -\Gamma_p P_{y_E} - P_{y_E}/T_2 + P_{x_E} \Delta\omega,$$

$$0 = -\Gamma_p P_{x_E} - P_{x_E}/T_2 - P_{y_E} \Delta\omega + P_{z_E} \omega_1.$$

Letting  $\Gamma = \Gamma_p + 1/T_2$ , we find that in the rotating frame

$$P_{x_E} = \frac{\Gamma_p}{\Gamma} \frac{\omega_1 \Delta\omega \sigma \cos\beta}{\Gamma^2 + \Delta\omega^2 + \omega_1^2},$$

$$P_{y_E} = \frac{\omega_1 \Gamma_p \sigma \cos\beta}{\Gamma^2 + \Delta\omega^2 + \omega_1^2},$$

$$P_{z_E} = \frac{\Gamma_p}{\Gamma} \frac{(\Gamma^2 + \Delta\omega^2) \sigma \cos\beta}{\Gamma^2 + \Delta\omega^2 + \omega_1^2}.$$

To calculate the light absorption we can either rotate  $\mathbf{P}$  to the laboratory frame or transform  $\hat{\mathbf{k}}$  to the rotating frame (the latter is easier). Thus,  $\hat{\mathbf{k}} \cdot \mathbf{P}$  yields a component of the light modulation in phase with  $B_1$  ("absorption" shape)

$$\frac{\omega_1 \Gamma_p \cos\beta \sin\beta}{\Gamma^2 + \Delta\omega^2 + \omega_1^2},$$

a component 90° out of phase with  $B_1$  ("dispersion" shape)

$$\frac{\Gamma_p}{\Gamma} \frac{\omega_1 \Delta\omega \cos\beta \sin\beta}{\Gamma^2 + \Delta\omega^2 + \omega_1^2},$$

and a dc term

$$\frac{\Gamma_p \cos^2\beta}{\Gamma} \left[ 1 - \frac{\omega_1^2}{\Gamma^2 + \Delta\omega^2 + \omega_1^2} \right].$$

The phase angle between  $B_1$  and  $\Delta I$  is thus

$$\tan\phi = \Delta\omega/\Gamma \approx \phi,$$

for  $\Delta\omega/\Gamma \ll 1$ . The sensitivity is then given by

$$\frac{d\phi}{d\Delta\omega} = 1/\Gamma.$$

In terms of a measured voltage  $V_{\text{in}}$  for the in-phase signal, the sensitivity of the out-of-phase signal  $V_{\text{out}}$  becomes

$$\frac{dV_{\text{out}}}{d\Delta\omega} = \frac{V_{\text{in}}}{\Gamma} \propto \frac{\Gamma_p}{\Gamma} \frac{\omega_1 \cos\beta \sin\beta}{\Gamma^2 + \omega_1^2}.$$

The conditions for maximum sensitivity are  $1/T_2 \approx \Gamma_p \approx \omega_1/2$  and  $\beta \approx \pi/4$ .

Note that if the oscillating field is not exactly perpendicular to the plane described by the static field and the light, the atomic oscillators can have a phase offset equal to the angular offset. This is illustrated as follows. Assume that the oscillating field is rotated by an angle ( $\delta\phi$ ) about the static field. This is equivalent to adding a phase offset in the rotating frame, which leads to an apparent frequency shift of  $\delta\phi/T_2$ .

## APPENDIX B: CALCULATION OF THE INDUCED LIGHT SHIFT ON A GROUND-STATE ENSEMBLE OF ATOMS

Consider an ensemble of ground-state atoms illuminated by electromagnetic radiation at a frequency  $\omega$ , electric field amplitude (squared)  $E^2$ , polarization vector  $\hat{\mathbf{e}}$ . (In this section, we use  $\omega$  to refer to the optical frequencies

and energy levels. Elsewhere,  $\omega$  refers to spin-precession frequencies.) The atoms have an excited state which is  $\Delta E = \hbar\omega_0$  above the ground state and which is coupled by electric dipole radiation to the ground state with a lifetime of  $1/\Gamma$ . The effective Hamiltonian of the light interacting with the atoms is<sup>4,38</sup>

$$\delta H = -E^2 \hat{\epsilon}^* \cdot \vec{\alpha} \cdot \hat{\epsilon},$$

where

$$\langle \mu' | \vec{\alpha}(\omega, \mathbf{v}) | \mu \rangle = -\frac{1}{\hbar} \sum_m \frac{\langle \mu' | \mathbf{D} | m \rangle \langle m | \mathbf{D} | \mu \rangle}{\omega - \omega_{m\mu} + \mathbf{k} \cdot \mathbf{v} + i\Gamma/2}$$

and  $\mathbf{D}$  is the electric dipole operator,  $\mathbf{k}$  is the propagation vector of the incident light,  $\mathbf{v}$  is the (thermal) velocity of the atoms,  $m$  labels the excited-state sublevels, and  $\mu$  labels ground-state sublevels. Note that, since we will be working in weak magnetic fields,  $\omega_{m\mu} = \omega_0$ .

To evaluate the total effect of the light on the ensemble of atoms it will be necessary to average over the spectral distribution of the incident light and over the velocities of the (thermal) atoms,

$$\vec{\alpha} = \int_{-\infty}^{\infty} \int_{-\infty}^{\infty} g(\omega) \vec{\alpha}(\omega, \mathbf{v}) N(\mathbf{v}) d^3v d\omega.$$

$N(\mathbf{v})d^3v$  is the Maxwellian velocity distribution,

$$N(\mathbf{v})d^3v = \left[ \frac{M}{2\pi RT} \right]^{3/2} \exp \left[ -\frac{Mv^2}{2RT} \right] d^3v,$$

where  $M$  is the gram weight of the atoms,  $T$  is the absolute temperature, and  $R$  is the gas constant.  $g(\omega)$  is the spectral density of the incident light

$$g(\omega) = \frac{2}{\pi^{1/2}} \exp \left[ -\frac{4(\omega - \omega_0)^2}{\Delta^2} \right],$$

where  $\Delta = 7.16 \times 10^{-7} \omega(T/A)^{1/2}$  with  $T$  the apparent temperature of the source (about 1000 K by Fabry-Perot measurements), and  $A$  the atomic weight of the radiating atoms (amu).

The integration was performed numerically (a simple rectangle rule integration) on a computer, first over the velocity for  $-3v_{\text{rms}} < v < 3v_{\text{rms}}$ , where  $v_{\text{rms}}$  is the rms velocity of the absorbing atoms (6000 steps) then over  $\omega$  for  $-3\Delta < \omega - \omega_0 < 3\Delta$  (150 steps). The results of the integration for the various lines of several Hg isotopes subjected to <sup>200</sup>Hg and <sup>204</sup>Hg lamps are given in Table VI. The overlap refers to the imaginary part of the integral

(depopulation pumping), and the dispersion to the real part (virtual light shift). We will eventually normalize the results of the dispersion integrals to the <sup>204</sup>Hg on <sup>199</sup>Hg dispersion value.

The effect of the light on the atoms can then be written as

$$\delta H = \delta E - i\hbar(\delta\Gamma/2),$$

where  $\delta E$  represents the virtual light shift and  $\delta\Gamma/2$  the depopulation pumping rate. The matrix representation of  $\delta H(\vec{\alpha})$  can be worked out in the ground-state Zeeman basis by using the Wigner-Eckart theorem to evaluate the matrix elements of  $\mathbf{D}$  (the electric dipole-moment operator) in terms of the reduced matrix element and 3- $j$  symbols,

$$\langle F_g \mu | D_i | F_e m \rangle = (-1)^{F_g - \mu} \langle F_g || D_i || F_e \rangle \begin{pmatrix} F_g & 1 & F_e \\ -\mu & i & m \end{pmatrix},$$

which simplifies the evaluation of

$$\sum_{i,j} \sum_m \langle \mu | e_i^* D_i | m \rangle \langle m | e_j D_j | \mu' \rangle.$$

Here  $m$  labels an excited state ( $F_e$ ) Zeeman level,  $\mu, \mu'$  label ground-state ( $F_g$ ) Zeeman levels,  $e_i, D_i$  ( $i = +1, 0, -1$ ) are the spherical vector representations of the light polarization state vector and the electric dipole-moment operator, respectively,<sup>19</sup>

$$e_{\pm 1} = \mp \frac{\sqrt{2}}{2} (e_x \mp i e_y),$$

$$e_0 = e_z,$$

$$D_{\pm 1} = \mp \frac{\sqrt{2}}{2} (D_x \pm i D_y),$$

$$D_0 = D_z,$$

and  $\mathbf{D} = e\mathbf{r}$ .

For the spin- $\frac{3}{2}$  <sup>201</sup>Hg atoms in the Zeeman basis, the effective Hamiltonian is represented by a  $4 \times 4$  matrix. Note that this matrix must be evaluated for each transition to the excited state because there is a different  $F_e$  (excited-state total angular momentum), overlap, and dispersion for each possible transition to the excited state for incident radiation from a particular lamp.

$\delta H$  is then expanded in terms of irreducible spherical tensors which are represented in the Zeeman basis by

TABLE VI. Dispersion overlaps.

Hg isotope	$F_e$	$F_g$	Line (mK)	Lamp isotope	$F_e$	$F_g$	Line (mK)	Overlap	Dispersion
201	1/2	3/2	229.40	200	1/1	0/0	-160.40	-0.377 506E+00	-0.656 263E+04
201	3/2	3/2	-22.60	200	1/1	0/0	-160.40	-0.886 290E+01	-0.197 440E+05
201	5/2	3/2	-489.30	200	1/1	0/0	-160.40	-0.535 151E+00	+0.780 126E+04
201	5/2	3/2	-489.30	204	1/1	0/0	-511.10	-0.774 692E+05	-0.437 513E+05
199	3/2	1/2	224.60	200	1/1	0/0	-160.40	-0.387 196E+00	-0.664 568E+04
199	1/2	1/2	-514.30	200	1/1	0/0	-160.40	-0.460 194E+00	+0.723 979E+04
199	1/2	1/2	-514.30	204	1/1	0/0	-511.10	-0.956 824E+00	+0.737 660E+04

$(2F+1) \times (2F+1)$  matrices for a ground state with total angular momentum  $F$ . For the present analysis, we need only consider the diagonal matrices (in the rotating frame the off-diagonal elements oscillate and do not lead to pumping or energy shifts). These matrices are given by<sup>38</sup>

$$T_{L,M}(F) = \sum_m |F, m\rangle \langle F, m-M| (2L+1)^{1/2} (-1)^{F-m} \\ \times \begin{pmatrix} F & F & L \\ m & M-m & -M \end{pmatrix}.$$

For  $M=0$  and  $F=\frac{3}{2}$  we find

$$T_{00}(\frac{3}{2}) = \begin{pmatrix} \frac{1}{2} & 0 & 0 & 0 \\ 0 & \frac{1}{2} & 0 & 0 \\ 0 & 0 & \frac{1}{2} & 0 \\ 0 & 0 & 0 & \frac{1}{2} \end{pmatrix}, \\ T_{10}(\frac{3}{2}) = \frac{1}{2\sqrt{5}} \begin{pmatrix} 3 & 0 & 0 & 0 \\ 0 & 1 & 0 & 0 \\ 0 & 0 & -1 & 0 \\ 0 & 0 & 0 & -3 \end{pmatrix}, \\ T_{20}(\frac{3}{2}) = \begin{pmatrix} \frac{1}{2} & 0 & 0 & 0 \\ 0 & -\frac{1}{2} & 0 & 0 \\ 0 & 0 & -\frac{1}{2} & 0 \\ 0 & 0 & 0 & \frac{1}{2} \end{pmatrix}, \quad (\text{B1})$$

and

$$T_{30}(\frac{3}{2}) = \frac{1}{2\sqrt{5}} \begin{pmatrix} 1 & 0 & 0 & 0 \\ 0 & -3 & 0 & 0 \\ 0 & 0 & 3 & 0 \\ 0 & 0 & 0 & -1 \end{pmatrix}.$$

For  $M=0$  and  $F=\frac{1}{2}$  we find

$$T_{00}(\frac{1}{2}) = \frac{1}{\sqrt{2}} \begin{pmatrix} 1 & 0 \\ 0 & 1 \end{pmatrix}, \\ T_{10}(\frac{1}{2}) = \frac{1}{\sqrt{2}} \begin{pmatrix} 1 & 0 \\ 0 & -1 \end{pmatrix}.$$

Any tensor operator (up to order  $2F$ ) can be expanded in terms of these tensor operators:<sup>38</sup>

$$O = \sum_{LM} O_{LM}(F) T_{LM}(F),$$

where

$$O_{LM}(F) = \text{Tr}[O T_{LM}^\dagger(F)].$$

Thus, the diagonal part of  $\bar{\alpha}$  can be easily expanded in terms of the  $T_{L0}$ . We find that the octupole component is zero (as it should be) in all cases. The scalar part ( $L=0$ )

is uninteresting. The dipole and quadrupole components will in general be nonzero for the spin- $\frac{3}{2}$  case, while only the dipole part will be nonzero for the spin- $\frac{1}{2}$  case. These components of  $\delta H$  give the light-induced dipole and quadrupole energy shifts of the ground-state ensemble.

For the present, we are interested in the virtual light shift,  $\delta E$ . The total light-shift Hamiltonian ( $H_L$ ) for the  $^1S_0$  Hg atoms with nuclear spin  $I$  illuminated by resonance radiation which couples to the  $^3P_1$  excited state is given by (up to a multiplicative constant)

$$H_L = \delta E = \sum_{F_e} \delta E(F_e) D_{\text{disp}}(F_e),$$

where  $F_e$  is an excited-state hyperfine level allowed by electric dipole selection rules,  $\delta E(F_e)$  is the matrix representation of the light shift resulting from coupling the ground state to  $F_e$  and  $D_{\text{disp}}(F_e)$  is the dispersion integral (Table VI) for the incident radiation of interest combined with the energy separation between the ground state and  $F_e$ . Note that  $H_L$  is readily determined up to a multiplicative constant for any  $I$  because the reduced matrix element is independent of  $I$ .<sup>20</sup> A remarkable fact is that this multiplicative constant is independent of  $I$ , as well. This same multiplicative constant times  $\delta\Gamma$  gives the depopulation pumping rate ( $\Gamma_p$ ),

$$\Gamma_p = (1/G) \text{Tr}(\delta\Gamma),$$

where  $G$  is the ground-state degeneracy.<sup>4</sup> Thus, if we know the light shift on  $^{199}\text{Hg}$  atoms due to resonance light from some particular isotope, we can determine the light shift on  $^{201}\text{Hg}$  atoms and the pump rate of both (or any other combination).

The results of the calculations for  $H_L$  will now be presented. For  $^{200}\text{Hg}$  resonance light on  $^{201}\text{Hg}$ , the dipole and quadrupole energy shifts,  $H_L = E_d + E_q$  are given by

$$E_d = -0.485e_d T_{10}(\frac{3}{2}), \quad E_q = 0.122e_q T_{20}(\frac{3}{2}), \quad (\text{B2})$$

where  $e_d = e_{+1}^2 - e_{-1}^2$  is the dipole component of the incident light and

$$e_q = e_{+1}^2 + e_{-1}^2 - 2e_0^2 = 1 - 3e_0^2$$

is the quadrupole component of the light. For 200 on 199,  $H_L = E_d$  with

$$E_d = 0.339e_d T_{10}(\frac{1}{2}). \quad (\text{B3})$$

For 204 on 201,  $H_L = E_d + E_q$  with

$$E_d = 0.663e_d T_{10}(\frac{3}{2}), \quad E_q = -0.098e_q T_{20}(\frac{3}{2}). \quad (\text{B4})$$

For 204 on 199,  $H_L = E_d$  with

$$E_d = e_d T_{10}(\frac{1}{2}) / 3\sqrt{2}. \quad (\text{B5})$$

All of these energies have been normalized to the 204 on 199 dispersion integral.

- <sup>1</sup>N. F. Ramsey, *Molecular Beams* (Oxford University Press, London, 1956).
- <sup>2</sup>A. Abragam, *The Principles of Nuclear Magnetism* (Clarendon, Oxford, 1961).
- <sup>3</sup>T. P. Das and E. L. Hahn, *Nuclear Quadrupole Resonance Spectroscopy* (Academic, New York, 1958).
- <sup>4</sup>W. Happer, *Rev. Mod. Phys.* **44**, 169 (1972).
- <sup>5</sup>P. A. Heimann, *Phys. Rev. A* **23**, 1204 (1981).
- <sup>6</sup>Z. Wu, W. Happer, and J. Daniels, *Phys. Rev. Lett.* **59**, 1480 (1987); (unpublished).
- <sup>7</sup>S. K. Lamoreaux, J. P. Jacobs, B. R. Heckel, F. J. Raab, and E. N. Fortson, *Phys. Rev. Lett.* **57**, 3125 (1986).
- <sup>8</sup>S. K. Lamoreaux, Ph.D. thesis, University of Washington, Seattle, 1986.
- <sup>9</sup>S. J. Lipson, G. D. Fletcher, and D. J. Larson, *Phys. Rev. Lett.* **57**, 567 (1986).
- <sup>10</sup>B. S. Mathur, H. Y. Tang, and W. Happer, *Phys. Rev. A* **2**, 648 (1970).
- <sup>11</sup>H. G. Dehmelt, *Phys. Rev.* **105**, 1487 (1957).
- <sup>12</sup>H. G. Dehmelt, *Phys. Rev.* **105**, 1924 (1957).
- <sup>13</sup>A. L. Bloom, *Appl. Opt.* **1**, 651 (1962).
- <sup>14</sup>R. D. Reimann, Ph.D. thesis, University of Washington, Seattle, 1973.
- <sup>15</sup>B. Cagnac and G. Lemeignan, *C. R. Acad. Sci.* **264**, 1850 (1967).
- <sup>16</sup>I. E. Grinko, V. F. Terzeman, Y. M. Petrukhov, and I. A. Shushpanov, *Opt. Spektrosk.* **31**, 6 (1971).
- <sup>17</sup>F. C. Fehsenfeld, K. M. Evenson, and H. P. Broida, *Rev. Sci. Instrum.* **36**, 294 (1965).
- <sup>18</sup>M. Kasha, *J. Opt. Soc. Am.* **38**, 929 (1948).
- <sup>19</sup>A. Messiah, *Quantum Mechanics* (Wiley, New York, 1966).
- <sup>20</sup>M. E. Rose, *Elementary Theory of Angular Momentum* (Wiley, New York, 1957).
- <sup>21</sup>W. Happer, *Phys. Rev. B* **1**, 2203 (1970).
- <sup>22</sup>J. H. DeBoer, *Dynamical Character of Adsorption* (Oxford, New York, 1963).
- <sup>23</sup>C. Cohen-Tannoudji, *Ann. Phys. (Paris)* **7**, 423 (1962).
- <sup>24</sup>M. A. Bouchiat, *J. Phys. (Paris)* **244**, 379 (1963); **34**, 611 (1963).
- <sup>25</sup>C. Cohen-Tannoudji, *J. Phys. (Paris)* **24**, 653 (1963).
- <sup>26</sup>P. A. Heimann, *Phys. Rev. A* **23**, 1204 (1981); P. A. Heimann, I. A. Greenwood, and J. H. Simpson, *ibid.* **23**, 120 (1981).
- <sup>27</sup>C. M. Will, *Theory and Experiment in Gravitational Physics* (Cambridge University Press, New York, 1981).
- <sup>28</sup>M. P. Haugen, *Ann. Phys. (N.Y.)* **118**, 156 (1979).
- <sup>29</sup>V. W. Hughes, H. G. Robinson, and V. Beltran-Lopez, *Phys. Rev. Lett.* **4**, 342 (1960); S. A. Lewis, W. L. Williams, and V. W. Hughes, *Bull. Am. Phys. Soc.* **11**, 121 (1966); W. L. Williams, Ph.D. thesis, Yale University, 1966.
- <sup>30</sup>R. W. P. Drever, *Philos. Mag.* **6**, 683 (1961).
- <sup>31</sup>J. D. Prestage, J. J. Bollinger, W. M. Itano, and D. J. Wineland, *Phys. Phys. Rev. Lett.* **54**, 2387 (1985).
- <sup>32</sup>A. P. Leitner and D. L. Lee, *Phys. Rev. D* **8**, 364 (1973).
- <sup>33</sup>P. R. Bevington, *Data Reduction and Error Analysis for the Physical Sciences* (McGraw-Hill, New York, 1969).
- <sup>34</sup>E. Riis *et al.*, *Phys. Rev. Lett.* **60**, 81 (1988).
- <sup>35</sup>J. Leitner and S. Okubo, *Phys. Rev.* **136**, B1542 (1964).
- <sup>36</sup>N. D. Hari Dass, *Phys. Rev. Lett.* **36**, 393 (1976); *Ann. Phys. (N.Y.)* **107**, 337 (1977).
- <sup>37</sup>R. Golub, *Inst. Phys. Conf. Ser.* **42**, 104 (1978).
- <sup>38</sup>W. Happer and B. S. Mathur, *Phys. Rev.* **163**, 12 (1967).